Electron Transfer in Mixed-Valence $[Fe^{III}_2Fe^{II}O(O_2CCH_3)_6(3\text{-Cl-py})_3]\cdot 3\text{-Cl-py}$: Effects of a Crystallographic Phase Transition and Conversion of Solvate and Ligand Molecules from Statically Disordered to Dynamically Disordered on the Valence Detrapping

Chi-Cheng Wu,[1] Sheri A. Hunt,[1] Peter K. Gantzel,[1] Philipp Gütlich,[2] and David N. Hendrickson*,[1]

Department of Chemistry-0358, University of California at San Diego, La Jolla, California 92093-0358, and Institut für Anorganische und Analytische Chemie, Johannes Gutenberg-Universität, D-55099 Mainz, Germany

Received January 10, 1997[⊗]

A crystallographic phase transition involving changes in the solvate molecule has been found for mixed-valence $[Fe_3O(O_2CCH_3)_6(3\text{-Cl-py})_3]\cdot 3\text{-Cl-py}$ (**1**), where 3-Cl-py is 3-chloropyridine. Single-crystal X-ray structures were determined at 300, 228, 200, 169, and 122 K for complex **1**. At 300, 228, and 200 K the crystal is monoclinic, space group $P2_1/c$, whereas at 169 and 122 K it is triclinic, space group $P\bar{1}$. Determinations of the unit cell parameters at several temperatures shows that a reversible crystallographic phase transition between the monoclinic and triclinic forms occurs at ∼200 K. Complex **1** crystallizes in the monoclinic space group $P2_1/c$ at 300 K, having a unit cell with $a = 21.212(8)$ Å, $b = 8.434(2)$ Å, $c = 23.676(3)$ Å, and $Z = 4$. Refinement with 5702 observed $[F_o \geq 4\sigma(F_o)]$ reflections gave $R = 0.0542$ and $R_w = 0.0937$. Complex **1** crystallizes in the triclinic space group $P\bar{1}$ at 122 K, having a unit cell with $a = 20.983(11)$ Å, $b = 8.360(4)$ Å, $c = 23.293(10)$ Å, and $Z = 4$. At 300 K there is one somewhat asymmetric Fe_3O complex in the structure. The core dimensions in the Fe_3O complex at 300 K indicate that the complex is becoming almost valence-detrapped. At 122 K there are two different Fe_3O complexes in the unit cell, both of which are similar in dimensions. As the temperature is decreased from 300 to 122 K, each Fe_3O complex becomes more and more distorted in an equilateral triangle. At 122 K one iron ion in each Fe_3O complex clearly is a high-spin Fe^{II} ion and the other two are high-spin Fe^{III} ions. There are significant changes in the nature of the 3-Cl-py solvate molecules above and below the phase transition that are likely important in controlling the valence detrapping. At 122 K there are two different Fe_3O complexes, each with their nearby 3-Cl-py solvate molecules in one position. There are three different phases: a monoclinic one with all solvate molecules disordered, a second triclinic phase at 169 K with half of the solvate molecules disordered, and a third triclinic phase at 122 K with all solvate molecules statically ordered. ^{57}Fe Mössbauer spectra taken in the 110−293 K range show that complex **1** converts from valence-trapped at 110 K to become detrapped by 293 K, where a single quadrupole-split doublet is seen. Throughout the 140−230 K range it was necessary to employ one Fe^{III} doublet and two Fe^{II} doublets to fit each Mössbauer spectrum. It is shown that the two Fe^{II} doublets likely arise from Fe_3O complexes experiencing the different disordered solvate environments described above. Thus, while the ∼200 K structural phase transition involving the solvate molecules does not precipitously lead to an increase in the rate of electron transfer in Fe_3O complexes in **1**, it is clear that the changes seen in the solvate molecules from X-ray structures do play a major role in the valence detrapping in complex **1**.

Introduction

Electron transfer reactions are all pervasive in chemistry.[3] Considerable insight about intramolecular electron transfer has been gained from the study of mixed-valence transition metal complexes in the solid state. Recent studies of mixed-valence trinuclear iron acetate[4] and dinuclear biferrocenium[5] complexes have shown that the detailed nature of the solid state environment about the mixed-valence complex can be the most important factor in determining the rate of intramolecular electron transfer.

Several factors such as the nature of the solvate molecule S and the crystal symmetry influence the rate of intramolecular

⊗ Abstract published in *Advance ACS Abstracts,* September 1, 1997.

(1) University of California at San Diego.

(2) Johannes-Gutenberg Universität.

(3) Recent reviews: (a) DeVault, D. *Quantum-Mechanical Tunneling in Biological Systems,* 2nd ed.; Cambridge University Press: Cambridge, U.K., 1984. (b) Cannon, R. D. *Electron Transfer Reactions*; Butterworths: Boston, MA, 1980. (c) Marcus, R. A.; Sutin, N. *Biochim. Biopys. Acta* **1985**, *811*, 265. (d) Mikkelsen, K. V.; Ratner, M. A. *Chem. Rev.* **1987**, *87*, 113. (e) Cannon, R. D. In *Encyclopedia of Inorganic Chemistry*; King, R. B., Ed.; J. Wiley & Sons: New York, 1994; Vol. 3, pp 1098−1111.

(4) (a) Oh, S. M.; Wilson, S. R.; Hendrickson, D. N.; Woehler, S. E.; Wittebort, R. J.; Inniss, D.; Strouse, C. E. *J. Am. Chem. Soc.* **1987**, *109*, 1073. (b) Jang, H. G.; Wittebort, R. J.; Sorai, M.; Kaneko, Y.; Nakano, M.; Hendrickson, D. N. *Inorg. Chem.* **1992**, *31*, 2265. (c) Jang, H. G.; Geib, S. J.; Kaneko, Y.; Nakano, M.; Sorai, M.; Rheingold, A. L.; Montez, B.; Hendrickson, D. N. *J. Am. Chem. Soc.* **1989**, *111*, 173. (d) Woehler, S. E.; Wittebort, R. J.; Oh, S. M.; Kambara, T.; Hendrickson, D. N.; Inniss, D.; Strouse, C. E. *J. Am. Chem. Soc.* **1987**, *109*, 1063. (e) Oh, S. M.; Hendrickson, D. N.; Hassett, K. L.; Davis, R. E. *J. Am. Chem. Soc.* **1984**, *106*, 7984. (f) Oh, S. M.; Hendrickson, D. N.; Hassett, K. L.; Davis, R. E. *J. Am. Chem. Soc.* **1985**, *107*, 8009. (g) Kambara, T.; Hendrickson, D. N.; Sorai, M.; Oh, S. M. *J. Chem. Phys.* **1986**, *85*, 2895. (h) Nakamoto, T.; Katada, M.; Kawata, S.; Kitagawa, S.; Kikuchi, K.; Ikemoto, I.; Endo, K.; Sano, H. *Chem. Lett.* **1993**, 1463. (i) Nakamoto, T.; Katada, M.; Kawata, S.; Kitagawa, S.; Sano, H.; Konno, M. *Hyperfine Interact.* **1994**, *93*, 1567. (j) Hendrickson, D. N.; Oh, S. M.; Dong, T.-Y.; Kambara, T.; Cohn, M. J.; Moore, M. F. *Comments Inorg. Chem.* **1985**, *4*, 329. (k) Hendrickson, D. N. Electron Transfer in Mixed-Valence Complexes in the Solid State. In *Mixed-Valency Systems: Applications in Chemistry, Physics and Biology*; Prassides, K., Ed.; NATO ASI Series C: Mathematical and Physical Sciences, 343; Kluwer Academic Publishers: Dordrecht, The Netherlands, 1991; pp 67−90.

S0020-1669(97)00031-1 CCC: $14.00

electron transfer for mixed-valence μ_3-oxo-centered $[Fe_3O(O_2CR)_6(L)_3]\cdot S$ complexes in the solid state. Several general comments can be made. First, these mixed-valence Fe_3O complexes never become electronically delocalized. The ground-state potential-energy surface always has appreciable barriers between the different vibronic states. This has been established by careful studies[6] of variable-temperature IR data. When the temperature of the solid is increased from below ~100 K to temperatures near room temperature, several of these Fe_3O complexes convert from valence-trapped to valence-detrapped. In the detrapped mode, Fe_3O complexes have enough thermal energy to convert from one vibronic state to another; *i.e.*, intramolecular electron transfer occurs. Each Fe_3O converts from one vibronic state to another either by going over a potential-energy barrier or by tunneling through it.

Second, the solvate molecule S in crystals of these Fe_3O complexes has a pronounced effect on the rate of intramolecular electron transfer. If you maintain the same $[Fe_3O(O_2CR)_6(L)_3]$ molecule, but change the solvate molecule S, this can turn on or off electron transfer. In every case studied[4a−d] by ^2H NMR it has been shown for those complexes that convert from valence-trapped to valence-detrapped as the temperature is increased, the solvate molecules convert from static to dynamic in the crystal in the same temperature regime where the valence detrapping occurs. In one case,[6f,g] incoherent quasielastic neutron scattering data also indicated the onset of solvate molecule motion. Thus, when the solvate molecule becomes dynamic this affects the potential-energy surface of the Fe_3O complexes in the crystal. The environment is made to be more symmetric for each Fe_3O complex. In this situation, two, three, or four of the vibronic energy minima on the surface for each Fe_3O complex become equal or nearly equal in energy, and this facilitates electron transfer. It should be pointed out that recently it was shown[7] that Fe_3O complexes without solvate molecules, but with long-chain carboxylate ligands (*e.g.*, R is a C_{17} chain), can become valence-detrapped even though they do not have solvate molecules. It is likely that there is an onset of motion in the long-chain alkyl group that facilitates the onset of electron transfer. In fact, very recently Sato *et al.*[8] showed that hydrogen-bonding interactions involving the water solvates in $[Fe_3O(CH_2XCO_2)_6(H_2O)_3]\cdot nH_2O$ affect the local environment of the iron ions and the valence detrapping. In this case it is possible that at low temperatures the hydrogen bonding network is static, whereas at higher temperatures the protons in the hydrogen bonding network are dynamic.

A third general observation about valence detrapping in Fe_3O complexes is that the conversion from valence-trapped to valence-detrapped occurs in an order−disorder phase transition. The main evidence for the presence of phase transitions has come from adiabatic heat capacity studies.[9] Heat capacity effects are seen in the temperature regime where ^{57}Fe Mössbauer spectra show valence detrapping of the Fe_3O complexes. The heat capacity data show that the valence detrapping conversion is entropy driven. It is a combination of entropy gain from the Fe_3O complex interconverting between several vibronic states together with entropy gain from the onset of motion of the S solvate molecules. More direct evidence for the presence of phase transitions could come from variable-temperature X-ray diffraction studies. In some cases,[4a,8] variable-temperature single-crystal X-ray structural data have shown that there is no change in the space group from the valence-trapped to the valence-detrapped form. This is possible in an order−disorder phase transition. In one case, single-crystal X-ray data have shown[4d] that $[Fe_3O(O_2CCH_3)_6(py)_3]\cdot py$, where py is pyridine, does undergo a crystallographic phase transition in the valence detrapping. This complex consists of Fe_3O molecules stacked one upon each other. Above 190 K the crystal of the py complex has a C_3 axis, but below 190 K the C_3 axis disappears. There is a heat capacity effect at this temperature and ^{57}Fe Mössbauer data show that the valence detrapping culminates at 190 K.

There is a fourth observation on Fe_3O complexes that is not yet general. In some cases,[8,9] it has been shown that as the temperature of a Fe_3O complex is increased the ^{57}Fe Mössbauer spectra change from a trapped signal with separate Fe^{II} and Fe^{III} signals to a spectrum with only one average quadrupole-split doublet. What is fascinating is that at intermediate temperatures there is no line broadening seen. Thus, the rate of intramolecular electron transfer is not just increasing with temperature and going through the ^{57}Fe Mössbauer "window". On the other hand, some variable-temperature Mössbauer spectra for mixed-valence Fe_3O complexes have been simulated[8,10] with a three-site relaxation model. The absence of line broadening in the ^{57}Fe Mössbauer spectra for the valence detrapping of mixed-valence biferrocene complexes has been firmly established in several cases.[5a,d,f]

In this paper, the first example of a crystallographic phase transition involving an order−disorder transformation of the S solvate molecule is reported for $[Fe_3O(O_2CCH_3)_6(3\text{-Cl-py})_3]\cdot$3-Cl-py (**1**), where 3-Cl-py is 3-chloropyridine. Variable-temperature single-crystal X-ray structural, ^{57}Fe Mössbauer, and ^2H NMR data are presented to determine the nature of structural

(5) (a) Dong, T.-Y.; Cohn, M. J.; Hendrickson, D. N.; Pierpont, C. G. *J. Am. Chem. Soc*. **1985**, *107*, 4777. (b) Cohn, M. J.; Dong, T.-Y.; Hendrickson, D. N.; Geib, S. J.; Rheingold, A. L. *J. Chem. Soc., Chem. Commun*. **1985**, 1095. (c) Dong, T.-Y.; Hendrickson, D. N.; Iwai, K.; Cohn, M. J.; Rheingold, A. L.; Sano, H.; Motoyama, I.; Nakashima, S. *J. Am. Chem. Soc*. **1985**, *107*, 7996. (d) Dong, T.-Y.; Hendrickson, D. N.; Pierpont, C. G.; Moore, M. F. *J. Am. Chem. Soc*. **1986**, *108*, 963. (e) Moore, M. F.; Wilson, S. R.; Cohn, M. J.; Dong, T.-Y.; Mueller-Westerhoff, U. T.; Hendrickson, D. N. *Inorg. Chem.* **1985**, *24*, 4559. (f) Dong, T.-Y.; Kambara, T.; Hendrickson, D. N. *J. Am. Chem. Soc*. **1986**, *108*, 4423. (g) Dong, T.-Y.; Kambara, T.; Hendrickson, D. N. *J. Am. Chem. Soc*. **1986**, *108*, 5857. (h) Sorai, M.; Nishimori, A.; Hendrickson, D. N.; Dong, T.-Y.; Cohn, M. J. *J. Am. Chem. Soc*. **1987**, *109*, 4266. (i) Kambara, T.; Hendrickson, D. N.; Dong, T.-Y.; Cohn, M. J. *J. Chem. Phys*. **1987**, *86*, 2362.

(6) (a) Cannon, R. D.; Montri, L.; Brown, D. B.; Marshall, K. M.; Elliott, C. M. *J. Am. Chem. Soc*. **1984**, *106*, 2591. (b) Meesuk, L.; Jayasooriya, U. A.; Cannon, R. D. *J. Am. Chem. Soc*. **1987**, *109*, 2009. (c) Wu, R.; Arap Koske, S. K.; White, R. P.; Anson, C. E.; Jayasooriya, U. A.; Cannon, R. D. *J. Chem. Soc., Chem. Commun*. **1994**, 1657. (d) White, R. P.; Wilson, L. M.; Williamson, D. J.; Moore, G. R.; Jayasooriya, U. A.; Cannon, R. D. *J. Chem. Soc., Chem. Commun*. **1994**,1657. (e) Cannon, R. D.; White, R. P. *Prog. Inorg. Chem*. **1988**, *36*, 195. (f) Cannon, R. D.; Jayasooria, U. A.; Arap Koske, S. K.; White, R. P.; Williams, J. H. *J. Am. Chem. Soc*. **1991**, *113*, 4158. (g) Cannon, R. D.; Jayasooria, U. A.; White, R. P. Inelastic Neutron Scattering Studies of Mixed-Valency Compounds. In *Mixed-Valency Systems: Applications in Chemistry, Physics and Biology*; Prassides, K., Ed.; NATO ASI Series C: Mathematical and Physical Sciences, 343; Kluwer Academic Publishers: Dordrecht, The Netherlands, 1991; pp 283−298.

(7) (a) Nakamoto, T.; Katada, M.; Sano, H. *Chem. Lett*. **1990**, 225. (b) Nakamoto, T.; Katada, M.; Sano, H. *Chem. Lett*. **1991**, 1323.

(8) Sato, T.; Ambe, F.; Endo, K.; Katada, M.; Maeda, H.; Nakamoto, T.; Sano, H. *J. Am. Chem. Soc*. **1996**, *118*, 3450.

(9) (a) Sorai, M.; Hendrickson, D. N. *Pure Appl. Chem*. **1991**, *63*, 1503. (b) Oh, S. M.; Kambara, T.; Hendrickson, D. N.; Sorai, M.; Kaji, K.; Woehler, S. E.; Wittebort, R. J. *J. Am. Chem. Soc*. **1985**, *107*, 5540. (c) Sorai, M.; KLaji, K.; Hendrickson, D. N.; Oh, S. M. *J. Am. Chem. Soc*. **1986**, *108*, 702. (d) Sorai, M.; Shiomi, Y.; Hendrickson, D. N.; Oh, S. M.; Kambara, T. *Inorg. Chem*. **1987**, *26*, 223. (e) Kaneko, Y.; Nakano, M.; Sorai, M.; Jang, H. G.; Hendrickson, D. N. *Inorg. Chem*. **1989**, *28*, 1067.

(10) (a) Dziobkowski, C. T.; Wrobleski, J. T.; Brown, D. B. *Inorg. Chem*. **1981**, *20*, 679. (b) Woehler, S. E.; Wittebort, R. J.; Oh, S. M.; Hendrickson, D. N.; Inniss, D.; Strouse, C. E. *J. Am. Chem. Soc*. **1986**, *108*, 2938.

Table 1. Variable-Temperature Unit Cell Parameters of $[Fe_3O(O_2CCH_3)_6(3\text{-Cl-py})_3]\cdot 3\text{-Cl-py}$ for Crystal Samples **1a** and **1b**

Crystal **1a**

	cooling cycle 1						cooling cycle 2	
	300 K	228 K	197 K	169 K	145 K	122 K	199 K	123 K
cryst system	monoclinic	monoclinic	monoclinic	triclinic	triclinic	triclinic	monoclinic	triclinic
a, Å	21.212(8)	21.172(9)	21.088(8)	21.058(12)	21.018(14)	20.983(11)	21.096(10)	20.995(12)
b, Å	8.434(2)	8.393(3)	8.376(3)	8.376(4)	8.368(5)	8.360(4)	8.381(4)	8.364(4)
c, Å	23.676(3)	23.515(8)	23.462(7)	23.398(11)	23.329(12)	23.293(10)	23.467(9)	23.298(10)
α, deg	90	90	90	90.46(4)	90.61(4)	90.67(3)	90	90.70(4)
β, deg	97.59(3)	97.74(3)	97.75(3)	97.88(4)	98.02(5)	98.15(4)	97.78(4)	98.15(4)
γ, deg	90	90	90	90.71(4)	91.01(5)	91.12(4)	90	91.08(4)
V, Å^3	4199(3)	4132(3)	4106(3)	4088(4)	4062(4)	4044(3)	4111(3)	4048(4)

Crystal **1b**

	219 K	209 K	200 K	189 K	180 K	170 K
cryst system	monoclinic	monoclinic	monoclinic	triclinic	triclinic	triclinic
a, Å	21.106(4)	21.098(4)	21.087(4)	21.080(8)	21.085(12)	21.073(8)
b, Å	8.391(2)	8.386(1)	8.384(1)	8.387(3)	8.383(5)	8.378(2)
c, Å	23.500(4)	23.484(3)	23.470(4)	23.467(7)	23.424(13)	23.393(7)
α, deg	90	90	90	90.15(3)	90.37(4)	90.54(2)
β, deg	97.68(2)	97.68(1)	97.71(2)	97.74(3)	97.79(5)	97.88(3)
γ, deg	90	90	90	90.11(3)	90.53(5)	90.78(3)
V, Å^3	4125(1)	4118(1)	4112(1)	4110(2)	4101(4)	4090(2)

phase transition seen at ∼200 K for complex **1**. It was important to determine how the structural phase transition involving the positioning of the solvate molecule S is related to the valence detrapping transformation in this complex. The absence of line broadening phenomenon seen in the ^{57}Fe Mössbauer spectra for certain Fe_3O complexes is also addressed.

Experimental Section

Compound Preparation. 3-Chloropyridine was dried by refluxing over BaO and then fractionally distilled under an argon atmosphere. Elemental analyses were performed by Oneida Research Service, Inc. Purified solvents and dried compounds were always stored and manipulated under an argon atmosphere.

$[Fe_3O(O_2CCH_3)_6(H_2O)_3]$. This mixed-valence compound was prepared according to a modification of a previously reported method.[11] A solution of 30 g (0.15 mol) of $FeCl_2\cdot 4H_2O$ in 150 mL of water was placed in a 500 mL three-neck flask. To this solution was added a suspension of 30 g (0.366 mol) of CH_3COONa in 90 mL (1.57 mol) of glacial acetic acid. The reaction mixture was heated at 70−75 °C under reflux for 2 h, with bubbling of a constant stream of air. The mixture was cooled to room temperature and the dark-brown precipitate was filtered off, washed with ethanol and ethyl ether, and dried under vacuum for 3 days. The yield was 15.6 g (52.7%). Anal. Calcd for $C_{12}H_{24}O_{16}Fe_3$: C, 24.35; H, 4.09; Fe, 28.31. Found: C, 24.09; H, 4.18; Fe, 27.89.

$[Fe_3O(O_2CCH_3)_6(3\text{-Cl-py})_3]\cdot 3\text{-Cl-py}$. The sample of this compound was prepared by dissolving 6.0 g (10.2 mmol) of $[Fe_3O(O_2CCH_3)_6(H_2O)_3]$ in 50 g of 3-chloropyridine and stirring the mixture for 1 h at 70−75 °C under an argon atmosphere. The warm solution (∼60 °C) was filtered and then slowly cooled to room temperature for crystallization. The black crystalline product was filtered off and washed with diethyl ether [yield was 3.2 g (57.5%)]. Anal. Calcd for $C_{32}H_{34}N_4Cl_4Fe_3O_{13}$: C, 38.78; H, 3.46; N, 5.65; Cl, 14.31; Fe, 16.81. Found: C, 38.69; H, 3.41; N, 5.76; Cl, 13.60; Fe, 17.54. The crystalline and single-crystal samples of $[Fe_3O(O_2CCD_3)_6(3\text{-Cl-py})_3]\cdot 3\text{-Cl-py}$ were prepared by the same method with the corresponding deuterated reagents purchased from Cambridge Isotope Labs.

Physical Measurements. Variable-Temperature ^{57}Fe Mössbauer Spectroscopy. Variable-temperature Mössbauer spectra were obtained in horizontal transmission geometry by using a conventional spectrometer operating in the constant acceleration mode. The source was ^{57}Co/Rh kept at room temperature. The samples were sealed in polished Plexiglas containers and mounted in a bath cryostat equipped with windows of nontransparent aluminated Mylar foil and filled with helium exchange gas. The temperature was measured with a calibrated Si diode. The temperature stability was ca. 0.1 K. Computer fittings of Mössbauer data to Lorentzian line shapes were carried out with the program MOSFUN (Mössbauer Spectra Fitting Program for Universal Theories).[12] The center shift values are reported relative to iron foil at 298 K but are not corrected for the temperature-dependent second-order Doppler shift.

Crystal Measurements, Data Collection, and X-ray Structure Refinements. Variable-temperature X-ray diffraction data were collected for $[Fe_3O(O_2CCH_3)_6(3\text{-Cl-py})_3]\cdot 3\text{-Cl-py}$ on a Siemens R3m/v automated diffractometer using graphite-monochromated Mo Kα radiation ($\lambda = 0.7107$ Å).

Crystallographic data were collected on two single crystals, a 0.4 × 0.9 × 0.6 mm crystal (**1a**) and a 0.3 × 0.6 × 0.7 mm crystal (**1b**), of complex **1** prepared from different reaction batches. Variable-temperature unit cell parameters listed in Table 1 were obtained by a least-squares fit to the automatically centered settings of 14 reflections. There was no evidence of twinning, and no change in the appearances of the crystal samples was noted during the experiments. However, a crystallographic phase transition has been found at ∼200 K. This phase transition was first observed in the cooling cycle 1 (Table 1) for data collections on crystal **1a**. The results of data collections and unit cell parameters at 300, 228, and 197 K for crystal **1a** are consistent with a monoclinic crystal system for complex **1**. As the crystal was further cooled to 169 K from 197 K, the reflection data could not be satisfactorily fitted to a monoclinic crystal system due to systematic changes in α and *γ* unit cell angles. At 169 K, the reflection data no longer show $I(hkl) = I(h\bar{k}l)$ monoclinic symmetry. There were also considerable and reversible changes (0.7−1.2°) of reflection line widths but no distinct line splitting, observed as the temperature of the crystal was lowered from 200 to 169 K. All of these results indicate a structural phase transition from high-temperature monoclinic to low-temperature triclinic crystal system. The data collection for crystal **1a** in the cooling cycle 1 was completed at 122 K, and then the crystal temperature was increased to 300 K before running the cooling cycle 2. There was no noticeable change of the crystal appearance after warming to room temperature again. The consistency for the results of data collection at 199 and 123 K in cycle 2 indicates that the crystallographic phase transition is a reversible process (see Table 1). Unit cell parameters at temperatures between 219 K and 170 K (Table 1) were also determined for crystal **1b** to study the reproducibility and investigate the details of the phase transition at ∼200 K.

The complete crystallographic data for complex **1** at 300, 228, 169, and 122 K were collected on crystal **1a**, whereas the data at 200 K

(11) Johnson, M. K.; Cannon, R. D.; Powell, D. B. *Spectrochim. Acta* **1982**, *38A*, 307.

(12) Müller, E. W. *Moessbauer Eff. Ref. Data J.* **1981**, *4*, 89.

Table 2. Summary of Crystal Data and Intensity Collection and Structure Refinement Details for $[Fe_3O(O_2CCH_3)_6(3\text{-Cl-py})_3]\cdot 3\text{-Cl-py}$ at 300, 228, 200, 169, and 122 K

	300 K	228 K	200 K	169 K	122 K
cryst sample	crystal **1a**	crystal **1a**	crystal **1b**	crystal **1a**	crystal **1a**
cryst system	monoclinic	monoclinic	monoclinic	triclinic	triclinic
space group	$P2_1/c$	$P2_1/c$	$P2_1/c$	$P\bar{1}$	$P\bar{1}$
a, Å	21.212(8)	21.172(9)	21.087(4)	21.058(12)	20.983(11)
b, Å	8.434(2)	8.393(3)	8.384(1)	8.376(4)	8.360(4)
c, Å	23.676(3)	23.515(8)	23.470(4)	23.398(11)	23.293(10)
α, deg	90	90	90	90.46(4)	90.67(3)
β, deg	97.59(3)	97.74(3)	97.710(1)	97.88(4)	97.74(3)
γ, deg	90	90	90	90.71(4)	91.12(4)
V, Å^3	4199(3)	4132(3)	4111.9(12)	4088(4)	4044(3)
Z	4	4	4	4	4
d(calcd), g/cm^3	1.569	1.595	1.602	1.612	1.629
cryst dimens, mm	0.4 × 0.9 × 0.6	0.4 × 0.9 × 0.6	0.3 × 0.6 × 0.7	0.4 × 0.9 × 0.6	0.4 × 0.9 × 0.6
radiation; λ, Å	Mo Kα; 0.710 73	Mo Kα; 0.710 73	Mo Kα; 0.710 73	Mo Kα; 0.710 73	Mo Kα; 0.710 73
scan speed, deg/min	constant; 19.53	constant; 19.53	constant; 10.19	constant; 19.53	constant; 19.53
scan mode	ω	ω	ω	ω	ω
scan limit, deg	$3 \le 2\theta \le 50.0$	$3 \le 2\theta \le 50.0$	$3 \le 2\theta \le 45.0$	$3 \le 2\theta \le 45.0$	$3 \le 2\theta \le 45.0$
R(int), %	2.22	1.81	1.45	3.58	2.77
no. of unique data	9533	7245	5357	10 657	10 540
no. of unique data for $F_o > 4\sigma(F_o)$	5702	5515	4302	8488	8372
no. of variables	505	505	505	976	854
R_F, %	5.42	4.51	4.21	6.65	6.62
R_{wF}, %	9.37	6.20	5.50	9.79	8.42
goodness of fit	1.27	1.35	1.36	2.22	2.45

were collected on crystal **1b**. Summaries of crystal data, intensity collection, and structure refinement are listed in Table 2. Data were corrected for Lorentz, polarization, and anomalous dispersion effects. The variable-temperature structures of complex **1** were solved by an automated interpreted Patterson procedure which located the Fe atoms followed by tangent expansion; the remaining non-hydrogen atoms were obtained from subsequent difference Fourier syntheses. Refinement of the structures included anisotropic temperature parameters for non-hydrogen atoms. Hydrogen atoms were incorporated as fixed idealized isotropic contributions [d(C−H) = 0.96 Å]. The final positional parameters for all refined atoms of complex **1** at 300 K are listed in Table 3. Selected bond distances and angles of the central atoms for complex **1** at all five temperatures are given in Table 4. The final positional parameters for complex **1** at 122 K are given in Table 5. Tables of positional parameters for the X-ray structures at 228, 200, and 169 K are available in the Supporting Information.

The 3-chloropyridine solvate molecule was found to be disordered in two resolvable orientations in both the monoclinic and triclinic crystal systems at 300, 228, 200, and 169 K. However, there is no evidence for disordered solvate molecule in the crystallographic data of complex **1** at 122 K. In the case of the two crystallographically different Fe_3O complexes of the triclinic unit cell at 169 K, only one of the two different Fe_3O complexes was found to be associated with disordered solvate molecules. Since the carbon and nitrogen atoms in the disordered 3-chloropyridine solvate molecule are indistinguishable, the disordered solvate molecule was modeled by two rigid chlorobenzene groups (C−C = 1.404 Å, C−H = 0.966 Å, C−Cl = 1.767 Å). The position and orientation of each disordered group were refined. In the final structure results, anisotropic temperature factors were refined and assigned to chlorine atoms in both groups and aromatic carbon atoms in one of the two disordered solvate groups, whereas a single isotropic group temperature factor was refined and assigned to the aromatic carbon atoms in the other disordered group. The total occupancy of the two groups was constrained to equal 1. The temperature-dependent ratios of the occupancy for the two disordered groups were determined by several least-squares fitting cycles. The first fitting model constrained the occupancy ratio for both disordered groups to be 50/50, and then the isotropic thermal coefficients of all aromatic carbon atoms in both groups were determined. In the next few least-squares cycles, by changing the occupancy ratio to adjust the isotropic thermal coefficients for both groups to be comparable, the final occupancy ratios were refined. After the ratio was determined, anisotropic thermal coefficients were introduced on the aromatic carbon atoms of one disordered solvate group in the fitting models. The final results of occupancy ratios for the disordered solvate group with anisotropic thermal coefficients and the group with single isotropic thermal coefficients were found to be 60/40 at 300 K, 70/30 at both 228 and 200 K, and 30/70 at 169 K.

All computations used the SHELXTL/PC library of crystallographic software (G. Sheldrick, Siemens, Madison, WI). Tables of detailed bond lengths and bond angles, anisotropic thermal parameters, hydrogen atom coordinates, and listings of structure factor amplitudes for both complexes **1** are available in the Supporting Information.

Magnetic Susceptibility Measurements. Variable-temperature magnetic susceptibilities of $[Fe_3O(O_2CCH_3)_6(3\text{-Cl-py})_3]\cdot 3\text{-Cl-py}$ were measured using a Quantum Design MPMS SQUID susceptometer. Data were collected on a powder sample (22.4 mg) and a single-crystal sample (29.4 mg) in the temperature range 5−320 K at an applied field of 10.0 kG. The powder sample was tightly wrapped in thin wax film to avoid sample torquing in the applied magnetic field. Single-crystal X-ray diffraction data were determined in order to orient a crystal so that the b axis of the unit cell was parallel to the applied field during the magnetic susceptibility measurements. Pascal's constants were used to estimate the diamagnetic correction that was subtracted from experimental molar susceptibility values to give the molar paramagnetic susceptibility data.

Solid-State ^{2}H NMR Spectroscopy. ^{2}H NMR experiments were performed on a single-crystal sample and a powder sample of $[Fe_3O(O_2CCD_3)_6(3\text{-Cl-py})_3]\cdot 3\text{-Cl-py}$ (**1**). The powder sample consisted of ∼50−70 mg of tightly packed microcrystalline material sealed into a NMR glass tube. The single-crystal spectra were collected on a 2.0 × 3.5 × 5.0 mm single crystal. The CD_3 deuterons were used to probe the symmetry of the Fe_3O triangle at temperatures above and below the structural phase transition temperature. All crystal phases and axes were determined with the aid of X-ray diffraction data. The single crystal was mounted with the crystallographic b axis parallel to the magnetic field direction. The ^{2}H NMR spectra were obtained on a home-built spectrometer with an 8.54 T magnet operating at a resonance frequency of 55.305 MHz. The probe was a single coil solenoid design with a 5 mm diameter. The pulse sequence used was $[(\pi/2)_x-\tau/2-(\pi)_y-\tau/2-(\pi/2)_y-\tau/2-(\pi)_y-\tau/2-$observe], which refocuses both the quadrupolar and paramagnetic interactions.[13] In this sequence the interval τ between pulses was 50 μs, whereas the $\pi/2$ pulses were 1.8 μs and π pulses were 3.6 μs. Echo decays were transferred to an off-line computer for processing with a software package from Hare Research Inc. Line shape simulations for spectra of the powder sample were performed with the program PMX4.[14] The PMX4 program incorporates a point dipole interaction for the through-space interaction

(13) Bayerl, T. M.; Bloom, M. *J. Magn. Reson.* **1990**, *88*, 257.
(14) Lin, T.-H.; Dinatale, J. A.; Vold, R. R. *J. Am. Chem. Soc.* **1994**, *116*, 2133.

Table 3. Positional Parameters for $[Fe_3O(O_2CCH_3)_6(3\text{-Cl-py})_3]\cdot 3\text{-Cl-py}$ at 300 K

atom	*x*/*a*	*y*/*b*	*z*/*c*
Fe(1)	0.6893(1)	0.8235(1)	0.2143(1)
Fe(2)	0.7928(1)	0.6602(1)	0.1395(1)
Fe(3)	0.8405(1)	0.8117(1)	0.2664(1)
Cl(1)	0.4274(1)	0.9041(5)	0.1174(1)
Cl(2)	0.8370(1)	0.0947(3)	0.0102(1)
Cl(3)	0.9768(1)	0.6913(2)	0.4904(1)
O(1)	0.7737(1)	0.7667(4)	0.2075(1)
O(2)	0.6708(2)	0.9242(5)	0.1353(2)
O(3)	0.7380(2)	0.8080(5)	0.0829(2)
O(4)	0.8705(2)	0.8023(4)	0.1287(2)
O(5)	0.8996(2)	0.9085(5)	0.2141(2)
O(6)	0.8128(2)	1.0377(4)	0.2853(2)
O(7)	0.7105(2)	1.0423(5)	0.2488(2)
O(8)	0.6475(2)	0.6127(5)	0.1855(2)
O(9)	0.7198(2)	0.4957(5)	0.1394(2)
O(10)	0.8521(2)	0.4922(5)	0.1807(2)
O(11)	0.8844(2)	0.5951(4)	0.2665(2)
O(12)	0.7930(2)	0.7285(5)	0.3310(2)
O(13)	0.6897(2)	0.7337(5)	0.2959(2)
N(1)	0.5891(2)	0.9014(6)	0.2198(2)
N(2)	0.8130(2)	0.5340(6)	0.0591(2)
N(3)	0.9206(2)	0.8607(5)	0.3370(2)
C(1)	0.5729(3)	0.9688(8)	0.2664(3)
C(2)	0.5112(3)	1.0245(9)	0.2700(3)
C(3)	0.4664(3)	1.0089(9)	0.2246(4)
C(4)	0.4825(3)	0.9362(10)	0.1765(3)
C(5)	0.5445(3)	0.8855(8)	0.1751(3)
C(6)	0.8159(3)	0.6155(8)	0.0111(3)
C(7)	0.8244(3)	0.5420(10)	−0.0401(3)
C(8)	0.8311(3)	0.3817(10)	−0.0411(3)
C(9)	0.8280(3)	0.2961(8)	0.0081(3)
C(10)	0.8190(3)	0.3764(7)	0.0578(3)
C(11)	0.9596(3)	0.9835(7)	0.3343(3)
C(12)	1.0072(3)	1.0227(8)	0.3788(3)
C(13)	1.0132(3)	0.9346(7)	0.4277(3)
C(14)	0.9722(3)	0.8078(7)	0.4297(2)
C(15)	0.9277(2)	0.7728(6)	0.3842(2)
C(16)	0.6953(3)	0.9041(7)	0.0902(2)
C(17)	0.6697(3)	1.0074(9)	0.0403(3)
C(18)	0.9028(2)	0.8962(6)	0.1617(2)
C(19)	0.9500(3)	0.9983(8)	0.1371(3)
C(20)	0.7589(3)	1.1047(6)	0.2738(3)
C(21)	0.7533(3)	1.2737(7)	0.2929(3)
C(22)	0.6699(3)	0.4965(7)	0.1611(2)
C(23)	0.6304(3)	0.3465(7)	0.1580(3)
C(24)	0.8815(2)	0.4863(6)	0.2304(2)
C(25)	0.9176(3)	0.3359(7)	0.2476(3)
C(26)	0.7346(3)	0.7036(7)	0.3337(2)
C(27)	0.7185(3)	0.6340(9)	0.3884(3)
C(28A)	0.4403(4)	0.1042(11)	0.5812(3)
C(29A)	0.3962	−0.0068	0.5961
C(30A)	0.3508	−0.0717	0.5539
C(31A)	0.3495	−0.0255	0.4967
C(32A)	0.3935	0.0855	0.4818
C(33A)	0.4389	0.1504	0.5241
Cl(4A)	0.4945	0.2905	0.5052
C(28B)	0.4010(7)	0.0782(19)	0.4808(5)
C(29B)	0.4471	0.1693	0.4585
C(30B)	0.4904	0.2598	0.4952
C(31B)	0.4876	0.2591	0.5542
C(32B)	0.4415	0.1680	0.5764
C(33B)	0.3982	0.0775	0.5397
Cl(4B)	0.3400	−0.0375	0.5678

of the deuteron with the magnetic moment associated with the unpaired electrons of the complex. The NMR simulations were carried out on IBM RISC 6000 workstation.

Results and Discussion

Crystallographic Phase Transition and Variable-Temperature Single-Crystal X-ray Structure of Complex 1. The unit cell parameters of complex **1** were determined at several temperatures. It will be shown that complex **1** converts from valence-trapped at low temperatures to valence-detrapped at room temperature and its crystal lattice undergoes a crystallographic phase transition from a triclinic crystal system at temperatures below ∼200 K to monoclinic at temperatures above ∼200 K. Variable-temperature crystallographic data for complex **1** were collected on two different crystals, labeled **1a** and **1b**, that were obtained from different reaction batches. A summary of the variable-temperature unit cell parameters for complex **1** is given in Table 1. At room temperature, complex **1** crystallizes in a monoclinic crystal system, in which both the α and γ angles are 90°, whereas at temperatures below ∼200 K the crystal system of complex **1** changes to a triclinic one. Figure 1 shows that there are relatively abrupt changes in the unit cell parameters α, β, and γ occurring at ∼195 K. There are also smaller kinks at ∼195 K in the plots of *a*, *b*, and *c* versus temperature. The data shown in Figure 1 and given in Table 1 were obtained by first cooling crystal **1a** from 300 to 122 K (● points) and then warming the crystal to room temperature, followed by a second cooling cycle (○ points) with data measured at 199 and 123 K. The absence of any deterioration of the crystal quality can be judged by the consistency of results collected at ∼197 and ∼122 K in the two cooling cycles. This indicates that the structural phase transition is a reversible process. It was noted that there was reflection line broadening observed when the temperature was lowered from 200 to 169 K. When the crystal passes through the phase transition, the reversible line width changes (from 0.7 to 1.2°) were not accompanied by any splitting, suggesting that some domain structures are formed in the crystal lattice such that any transformation strain is distributed throughout the crystal without fracturing.

To closely examine the phase transition another set of X-ray data was collected on a second crystal sample **1b**, as listed in Table 1 and plotted in Figure 1 (□). These results give a more precise temperature range (189−200 K) for the onset of the crystallographic phase transition. The data collected on crystal **1a** are reproducible on other crystal samples. In the range 122−200 K, the changes in α and γ are 0.67 and 1.12°, respectively. On the other hand, the variation of β angle within the same temperature range is only 0.40°. The relatively greater variations for the α and γ angles through the phase transition from monoclinic to triclinic crystal system indicate that the transformation of the unit cell mainly involves the tilting of the *b* axis from its original position where the *b* axis is orthogonal to the *ac* plane.

In addition to the determination of unit cell parameters, single-crystal X-ray structures of $[Fe_3O(O_2CCH_3)_6(3\text{-Cl-py})_3]\cdot 3\text{-Cl-py}$ (**1**) were also determined at 300, 228, 200, 169, and 122 K. A summary of the crystal data, intensity collection, and structure refinements for complex **1** are given in Table 2. In the high-temperature phase at 300, 228, and 200 K complex **1** crystallizes in the monoclinic space group $P2_1/c$ with four molecules in the unit cell. At these three temperatures the 3-Cl-py solvate molecule is disordered between two resolvable positions. The perspective views of the molecular structures of μ_3-oxo-bridged trinuclear complex with a disordered solvate molecule at 300 and 200 K are depicted in Figure 2. The final positional parameters of complex **1** at 300 K are given in Table 3. (Complete tables of positional parameters and bond distances and angles for all of the structures at 300, 228, and 200 K are available in the Supporting Information.)

As the temperature of the crystal is increased from 200 to 300 K, significant dimensional changes occur in the Fe_3O triangle. Selected bond distances and angles are given in Table

Table 4. Selected Bond Distances and Angles of the Central Atoms for $[Fe_3O(O_2CCH_3)_6(3\text{-Cl-py})_3]\cdot 3\text{-Cl-py}$ at 300, 228, 200, 169, and 122 K

Bond Distances (Å)

atoms	300 K	228 K	200 K	atoms	169 K	122 K
Fe(1)−O(1)	1.880(3)	1.866(3)	1.857(3)	Fe(1A)−O(1A)	1.849(5)	1.839(6)
Fe(2)−O(1)	1.933(3)	1.966(3)	1.994(3)	Fe(2A)−O(1A)	2.007(5)	2.043(6)
Fe(3)−O(1)	1.890(3)	1.873(3)	1.861(3)	Fe(3A)−O(1A)	1.855(5)	1.836(5)
				Fe(1B)−O(1B)	1.841(5)	1.838(1)
				Fe(2B)−O(1B)	1.990(5)	2.020(1)
				Fe(3B)−O(1B)	1.881(5)	1.853(1)
Fe(1)−O[a]	2.058	2.051	2.046	Fe(1A)−O[a]	2.049	2.042
Fe(2)−O[a]	2.081	2.092	2.101	Fe(2A)−O[a]	2.109	2.119
Fe(3)−O[a]	2.062	2.056	2.052	Fe(3A)−O[a]	2.041	2.039
				Fe(1B)−O[a]	2.042	2.037
				Fe(2B)−O[a]	2.100	2.107
				Fe(3B)−O[a]	2.056	2.047

Bond Angles (deg)

atoms	300 K	228 K	200 K	atoms	169 K	122 K
Fe(1)−O(1)−Fe(2)	119.8(2)	119.4(1)	118.9(1)	Fe(1A)−O(1A)−Fe(2A)	119.2(2)	118.6(3)
Fe(1)−O(1)−Fe(3)	121.0(2)	121.9(1)	122.7(2)	Fe(1A)−O(1A)−Fe(3A)	123.0(3)	124.0(3)
Fe(2)−O(1)−Fe(3)	119.2(2)	118.7(1)	118.4(2)	Fe(2A)−O(1A)−Fe(3A)	117.8(3)	117.4(3)
				Fe(1B)−O(1B)−Fe(2B)	119.3(2)	118.0(1)
				Fe(1B)−O(1B)−Fe(3B)	122.5(3)	123.3(1)
				Fe(2B)−O(1B)−Fe(3B)	118.2(3)	118.7(1)
Fe_3O-L_1[b]	6.7	7.4	7.9	$Fe_3O(A)-L_1$[b]	14.1	16.0
Fe_3O-L_2[b]	79.9	79.4	79.3	$Fe_3O(A)-L_2$[b]	77.5	77.3
Fe_3O-L_3[b]	76.6	76.5	76.2	$Fe_3O(A)-L_3$[b]	77.5	77.6
				$Fe_3O(B)-L_2$[b]	2.6	3.3
				$Fe_3O(B)-L_2$[b]	81.9	83.2
				$Fe_3O(B)-L_3$[b]	75.3	74.4

Table 5. Positional Parameters for $[Fe_3O(O_2CCH_3)_6(3\text{-Cl-py})_3]\cdot 3\text{-Cl-py}$ at 122 K

atom	*x*/*a*	*y*/*b*	*z*/*c*	atom	*x*/*a*	*y*/*b*	*z*/*c*	atom	*x*/*a*	*y*/*b*	*z*/*c*
Fe(1A)	0.6922(1)	0.8122(1)	0.2124(1)	C(17A)	0.6739(5)	1.0111(12)	0.0389(4)	N(1B)	0.5861(1)	0.5937(1)	−0.2817(1)
Fe(2A)	0.7970(1)	0.6463(1)	0.1355(1)	C(18A)	0.9077(4)	0.9003(10)	0.1620(4)	N(2B)	0.8112(1)	0.9680(1)	−0.4427(1)
Fe(3A)	0.8437(1)	0.8080(1)	0.2657(1)	C(19A)	0.9539(4)	1.0149(11)	0.1388(4)	N(3B)	0.9200(1)	0.6413(1)	−0.1614(1)
Cl(1A)	0.4325(1)	0.9634(4)	0.1119(1)	C(20A)	0.7640(4)	1.1018(11)	0.2739(4)	C(1B)	0.5692(1)	0.5094(1)	−0.2366(1)
Cl(2A)	0.8414(1)	0.0688(3)	0.0104(1)	C(21A)	0.7588(4)	1.2753(11)	0.2902(5)	C(2B)	0.5087(1)	0.4631(1)	−0.2316(1)
Cl(3A)	0.9816(1)	0.6914(3)	0.4939(1)	C(22A)	0.6689(4)	0.4772(10)	0.1596(4)	C(3B)	0.4593(1)	0.5012(1)	−0.2760(1)
O(1A)	0.7763(3)	0.7605(7)	0.2084(2)	C(23A)	0.6291(4)	0.3302(11)	0.1571(4)	C(4B)	0.4749(1)	0.5882(1)	−0.3221(1)
O(2A)	0.6734(3)	0.9123(7)	0.1338(2)	C(24A)	0.8864(4)	0.4808(10)	0.2321(4)	C(5B)	0.5398(1)	0.6325(1)	−0.3231(1)
O(3A)	0.7423(3)	0.8022(7)	0.0800(3)	C(25A)	0.9208(4)	0.3330(10)	0.2531(4)	C(6B)	0.8171(1)	0.8865(1)	−0.4921(1)
O(4A)	0.8763(3)	0.8017(7)	0.1268(3)	C(26A)	0.7376(4)	0.6950(10)	0.3339(4)	C(7B)	0.8271(1)	0.9595(1)	−0.5423(1)
O(5A)	0.9027(3)	0.9137(7)	0.2157(2)	C(27A)	0.7222(4)	0.6184(12)	0.3888(4)	C(8B)	0.8309(1)	1.1252(1)	−0.5436(1)
O(6A)	0.8166(3)	1.0343(7)	0.2871(3)	C(28A)	0.6082(2)	0.5808(5)	0.0175(2)	C(9B)	0.8249(1)	1.2091(1)	−0.4927(1)
O(7A)	0.7121(3)	1.0354(7)	0.2480(3)	C(29A)	0.6502	0.4681	0.0003	C(10B)	0.8150(1)	1.1266(1)	−0.4441(1)
O(8A)	0.6481(3)	0.6003(7)	0.1840(3)	C(30A)	0.6423	0.4123	−0.0566	C(11B)	0.9602(1)	0.5200(1)	−0.1652(1)
O(9A)	0.7196(3)	0.4769(7)	0.1380(2)	N(31A)	0.5925	0.4693	−0.0964	C(12B)	1.0084(1)	0.4819(1)	−0.1203(1)
O(10A)	0.8557(3)	0.4785(7)	0.1810(2)	C(32A)	0.5505	0.5820	−0.0792	C(13B)	1.0135(1)	0.5667(1)	−0.0692(1)
O(11A)	0.8891(3)	0.5975(7)	0.2676(3)	C(33A)	0.5584	0.6378	−0.0223	C(14B)	0.9717(1)	0.6906(1)	−0.0654(1)
O(12A)	0.7964(3)	0.7275(7)	0.3312(3)	Cl(4A)	0.5061	0.7782	−0.0009	C(15B)	0.9259(1)	0.7254(1)	−0.1119(1)
O(13A)	0.6917(3)	0.7257(7)	0.2948(2)	Fe(1B)	0.6878(1)	0.6693(1)	−0.2875 (1)	C(16B)	0.6898(1)	0.5874(1)	−0.4140(1)
N(1A)	0.5919(3)	0.8927(8)	0.2200(3)	Fe(2B)	0.7913(1)	0.8397(1)	−0.3639 (1)	C(17B)	0.6624(1)	0.4809(1)	−0.4641(1)
N(2A)	0.8161(3)	0.5166(8)	0.0558(3)	Fe(3B)	0.8393(1)	0.6861(1)	−0.2338 (1)	C(18B)	0.9012(1)	0.5949(1)	−0.3395(1)
N(3A)	0.9246(3)	0.8624(8)	0.3382(3)	Cl(1B)	0.4168(1)	0.6533(1)	−0.3762 (1)	C(19B)	0.9454(1)	0.4838(1)	−0.3634(1)
C(1A)	0.5769(4)	0.9501(10)	0.2703(4)	Cl(2B)	0.8310(1)	1.4156(1)	−0.4891 (1)	C(20B)	0.7566(1)	0.3854(1)	−0.2282(1)
C(2A)	0.5167(4)	1.0108(12)	0.2750(4)	Cl(3B)	0.9746(1)	0.8038(1)	−0.0018 (1)	C(21B)	0.7517(1)	0.2121(1)	−0.2148(1)
C(3A)	0.4704(4)	1.0170(11)	0.2274(4)	O(1B)	0.7719(1)	0.7266(1)	−0.2919(1)	C(22B)	0.6662(1)	0.9996(1)	−0.3384(1)
C(4A)	0.4870(4)	0.9607(12)	0.1758(4)	O(2B)	0.6653(1)	0.5719(1)	−0.3677(1)	C(23B)	0.6251(1)	1.1451(1)	−0.3423(1)
C(5A)	0.5468(4)	0.8979(10)	0.1728(4)	O(3B)	0.7338(1)	0.6844(1)	−0.4210(1)	C(24B)	0.8811(1)	1.0169(1)	−0.2669(1)
C(6A)	0.8155(4)	0.5915(11)	0.0047(4)	O(4B)	0.8695(1)	0.6887(1)	−0.373 (1)	C(25B)	0.9176(1)	1.1673(1)	−0.2460(1)
C(7A)	0.8223(4)	0.5141(12)	−0.0454 (4)	O(5B)	0.8978(1)	0.5851(1)	−0.2847(1)	C(26B)	0.7332(1)	0.7808(1)	−0.1640(1)
C(8A)	0.8293(4)	0.3500(12)	−0.0456(4)	O(6B)	0.8094(1)	0.4570(1)	−0.2149(1)	C(27B)	0.7161(1)	0.8459(1)	−0.1067(1)
C(9A)	0.8306(4)	0.2725(11)	0.0067(4)	O(7B)	0.7064(1)	0.4453(1)	−0.2552(1)	C(28B)	0.4382(2)	0.2014(6)	0.5767(2)
C(10A)	0.8227(4)	0.3577(11)	0.0561(4)	O(8B)	0.6470(1)	0.8805(1)	−0.3107(1)	C(29B)	0.4866	0.2871	0.5548
C(11A)	0.9650(4)	0.9875(10)	0.3361(4)	O(9B)	0.7158(1)	1.0029(1)	−0.3621(1)	C(30B)	0.4941	0.2720	0.4967
C(12A)	1.0130(4)	1.0294(11)	0.3811(4)	O(10B)	0.8512(1)	1.0110(1)	−0.3176(1)	N(31B)	0.4532	0.1711	0.4605
C(13A)	1.0199(4)	0.9377(10)	0.4317(4)	O(11B)	0.8850(1)	0.9028(1)	−0.2316(1)	C(32B)	0.4048	0.0853	0.4823
C(14A)	0.9781(4)	0.8077(10)	0.4321(3)	O(12B)	0.7926(1)	0.7659(1)	−0.1673(1)	C(33B)	0.3973	0.1005	0.5404
C(15A)	0.9312(4)	0.7717(10)	0.3862(3)	O(13B)	0.6877(1)	0.7476(1)	−0.2033(1)	Cl(4B)	0.3371	−0.0063	0.5676
C(16A)	0.6986(4)	0.8989(10)	0.0884(4)								

4 for all of the structure determinations. (Complete lists of bond distances and angles for all structures are available in the Supporting Information.) The Fe_3O triangle becomes more equilateral as the crystal is heated from 200 to 300 K. From

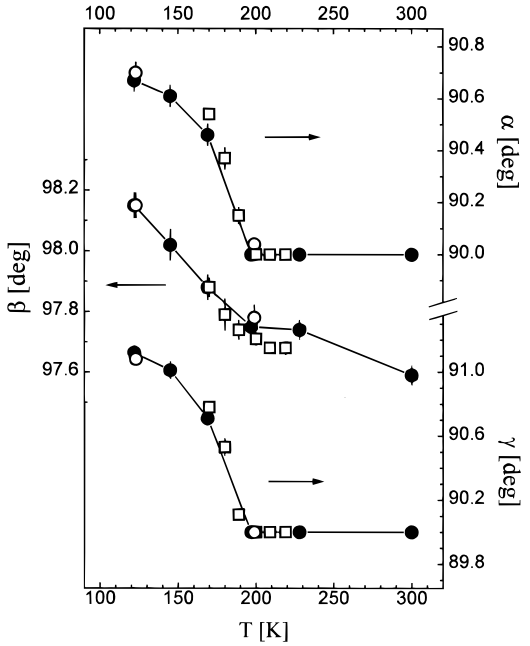

Figure 1. Temperature dependence of the interaxial angles (α, *β*, and *γ*) of the unit cell for $[Fe_3O(O_2CCH_3)_6(3\text{-Cl-py})_3]\cdot 3\text{-Cl-py}$ (**1**) from single-crystal X-ray structure determinations. Data are shown for the single-crystal sample **1a** from measurements in cooling cycle 1 (●) and cooling cycle 2 (○). Data are also shown for single crystal **1b** (□).

the comparison of the results of bond distances at low temperatures and previous studies on Fe_3O complexes, the iron ion Fe(2) can be assigned as the high-spin Fe^{II} ion. At 200 K the bond distances from each iron ion to the central oxide ion are appreciably different: Fe(1)−O(1) = 1.857(3) Å, Fe(2)−O(1) = 1.994(3) Å, and Fe(3)−O(1) = 1.861(3) Å. These three bond lengths are closer to being equal in the 300 K structure: Fe(1)−O(1) = 1.880(3) Å, Fe(2)−O(1) = 1.933(3) Å, and Fe(3)−O(1) = 1.890(3) Å. Each iron ion has a FeO_5N coordination geometry. The average ligand-to-iron bond length is also longer for the Fe(2) ion and this further confirms that Fe(2) is the "Fe^{II}" ion in the Fe_3O complex. From these crystal structure determinations it is clear that complex **1** is becoming almost valence-detrapped at 300 K.

There is no crystallographically imposed symmetry for the Fe_3O complex **1**. The planes of two of the three 3-Cl-py ligands incorporating the Cl(2) and Cl(3) atoms (Figure 2) are nearly perpendicular to the Fe_3O plane, while the plane of the third ligand with Cl(1) is nearly parallel to the Fe_3O plane (see Table 4). From room temperature to 200 K there is little variation in these three dihedral angles. The unique pattern of orientations for 3-Cl-py ligands in complex **1** is very similar to that reported[4f] for $[Fe_3O(O_2CCH_3)_6(4\text{-Et-py})_3]\cdot 4\text{-Et-py}$ (**2**) where the two 4-Et-py ligands coordinated to the two Fe^{III} ions are perpendicular to the Fe_3O plane and the plane of one disordered ligand bonded to the Fe^{II} ion is parallel. In all cases reported for mixed-valence Fe_3O complexes, the pyridine ligands are very nearly parallel to or perpendicular to the Fe_3O plane. All four possible isomers having 3, 2, 1, or 0 pyridine ligands in the Fe_3O plane have been reported.[4k] It also has been found that the conformation of the pyridine ligands is a major factor determining whether a Fe_3O complex can valence-detrap. When the three ligands are not symmetrically arranged, the three different vibronic states related to the three iron ions are not at the same energy. This will tend to trap a complex in one vibronic state. It was concluded[4f] that the onset of rotation of the unique 4-Et-py ligand in complex **2** affects the relative energies of the vibronic

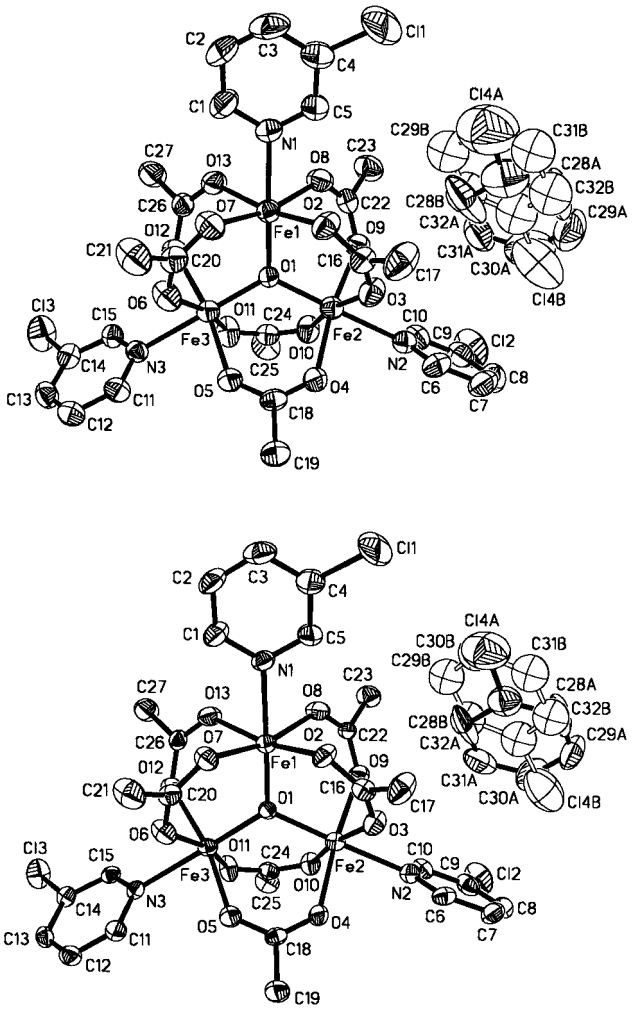

Figure 2. ORTEP plots of the molecular structure of the μ_3-oxo-bridged trinuclear complex accompanied by a disordered solvate molecule in $[Fe_3O(O_2CCH_3)_6(3\text{-Cl-py})_3]\cdot 3\text{-Cl-py}$ (**1**) at 300 K (top) and 200 K (bottom). At each temperature the solvate molecule was found to be disordered in two positions. In each drawing the 3-Cl-py solvate molecule that was found to have higher occupany is shown with filled-in dark bonds. Atoms are shown as 50% equiprobability ellipsoids.

states and leads to an increase in the rate of interconversion between vibronic states.

There is no *direct* evidence for 3-Cl-py ligand disorder in the X-ray structures of complex **1**. Nevertheless, complex **1** does convert from valence-trapped at low temperatures to valence-detrapped at high temperatures, as clearly shown in variable-temperature Mössbauer spectra. Close examination of the X-ray structural refinement data for the 3-Cl-py ligands gives some additional insight. The thermal displacement coefficients for atoms in the 3-Cl-py ligand with the Cl(1) atom are larger than those of the other two 3-Cl-py ligands. From 300 to 200 K, the equivalent isotropic displacement coefficients for the Cl(1) atom are 1.5−2.5 times larger than those of the other two chlorine atoms, Cl(2) and Cl(3), whereas the anisotropic thermal coefficients of the Cl(1) atom indicate that this chlorine atom is displaced upward or downward along a direction nearly perpendicular to the Fe_3O plane. This result suggests that the 3-Cl-py ligand with Cl(1) converts from statically to dynamically disordered (*i.e.*, fast 180° flips) to give a symmetric environment at high temperatures, where the three vibronic states are equivalent and thus complex **1** becomes valence-detrapped.

In addition to the influence from pyridine ligands, it is known[4k] that effects arising from solvate molecules, especially the onset of dynamics, are also important in controlling the rates

of intramolecular electron transfer in mixed-valence Fe_3O complexes. In all cases studied it has been found that when the solvate molecules are found to be disordered in more than one site in the X-ray crystal structures, dynamic solvate molecules are observed in the ^2H NMR study. For example, in the cases of $[Fe_3O(O_2CCH_3)_6(3\text{-Me-py})_3]\cdot$solvate, where the solvate molecule is either 3-Me-py or toluene, the solvate molecules are disordered between two positions, and the results of a ^2H NMR study have clearly shown the dynamic nature of these two solvate molecules.[4a]

In the high-temperature phase the 3-Cl-py solvate molecule in complex **1** is disordered between two positions, denoted as positions A and B. The pyridine rings of the two disordered solvate molecules are nearly lying on a plane (dihedral angle of ~15°); however, they are oriented in opposite directions with an overlap of the chlorine atom of one 3-Cl-py with the carbon atom at the para position of the other solvate molecule. In the refinement the total occupancy of these two disorder elements was fixed at one 3-Cl-py, but the occupancy ratio did not refine to 50/50. The occupancy ratio for the solvate at position A compared to that at position B is 60/40 at 300 K, and at 228 and 200 K it refined to 70/30. As can be seen in Figure 2, the thermal parameters for the atoms in the solvate molecules are appreciably larger than those of the Fe_3O molecule. The temperature dependence of occupancy ratio for disorder elements and the relatively large thermal coefficients for solvate atoms strongly suggest that the solvate molecules are dynamic in the 200−300 K range. In fact, as shown below, there is evidence that at temperatures below 200 K the 3-Cl-py solvate molecules become static.

In order to fully understand the structural phase transition found for complex **1**, it is necessary to examine the lattice packing of complex **1**. In the unit cell for a centrosymmetric $P2_1/c$ space group with $Z = 4$ there are two mirror image pairs of the asymmetric Fe_3O molecules and also mirror images of the different orientations for disordered solvate molecules associated with the Fe_3O molecules. A view of the packing arrangement of complex **1** is given in Figure 3. If the structure shown in Figure 2 is designated as the original Fe_3O molecular structure in $P2_1/c$ space group symmetry, then two molecules of this original structure are located at the corners of origin, (0, 0, 0) and (*a*, *b*, 0), in the unit cell and two mirror image molecules are located at the corners (*a*, *b*, *c*) and (0, 0, *c*) across the unit cell. Each Fe_3O molecule is accompanied by one nearest disordered solvate molecule. For instance, in Figure 3 the solvate molecules located at the center of the plot are associated with the mirror pair of Fe_3O complexes at the (0, 0, 0) and (*a*, *b*, *c*) corners in the unit cell.

There are two identifiable packing arrangements found for mixed-valence Fe_3O complexes. In one case the Fe_3O complexes are stacked one upon another with one solvate molecule sandwiched between two complexes. There are appreciable interactions between a given molecule in one stack and molecules in neighboring stacks. This occurs via $\pi-\pi$ intermolecular interactions of pyridine ligands. The other packing arrangement is that of layers of Fe_3O complexes. The solvate molecules are located in the layers in sites between three or four complexes. There is one significant difference between the "stacked" and "layered" packing arrangements. In the latter there are no appreciable intermolecular interactions between neighboring Fe_3O complexes. There are only weak van der Waals interactions between Fe_3O complexes in the "layered" packing.

In Figure 3a is shown a stereoview of the packing arrangement present in complex **1** at 300 K. Complex **1** has a "layered" structure. One "layer" includes six Fe_3O molecules and runs nearly parallel (dihedral angle of 20.5°) to the *ac* plane. At 300 K all of the solvate molecules are disordered in two positions. In Figure 3a it can be seen that the disordered solvate molecules interact with the 3-Cl-py ligands on nearby complexes.

In the low-temperature phase at 169 and 122 K complex **1** crystallizes in the triclinic space group $P\bar{1}$ with four molecules in the unit cell also. A summary of crystal data, intensity collection, and structure refinement for complex **1** at these two temperatures is also given in Table 2. The perspective views of the molecular structures of the μ_3-oxo-bridged trinuclear complex with a solvate molecule at 169 and 122 K are depicted in Figures 4 and 5. The final positional parameters of complex **1** at 122 K are listed in Table 5. (Complete tables of positional parameters and bond distances and angles for the 169 and 122 K structures are available in the Supporting Information.)

In the triclinic unit cell at both 169 and 122 K there are two crystallographically different Fe_3O molecules with dimensions close to a mirror image couple (Figure 4 and 5). Selected bond distances and angles are given in Table 4. These two unique Fe_3O(A) and Fe_3O(B) molecules are transformed from one of the two mirror image pairs in the monoclinic unit cell of the high-temperature $P2_1/c$ phase. In both Figures 4 and 5 the structure of the top molecule (A) is in fact converted from the designated original structure at high temperatures (≥200 K), whereas the structure of the bottom one (B) is from the mirror image molecule of the original. Although the structures of these two unique molecules are very similar to mirror images, there are also two other complexes that are exact mirror images of these two original unique molecules in the triclinic unit cell, due to the symmetry in the space group $P\bar{1}$. In other words, as the crystal undergoes the phase transition from a monoclinic to a triclinic cell, there are only some variations on orientations and details of dimensions in the Fe_3O molecules. However, as is visible in Figures 4 and 5, the structures and orientations of the 3-Cl-py solvate molecules associated with these two different Fe_3O molecular units are very different. These differences in solvate molecules are actually the major factors that differentiate the two different Fe_3O(A) and Fe_3O(B) molecules, as well as the structures at temperatures above and below the phase transition.

As shown in Figure 4, at 169 K the solvate molecule associated with the top Fe_3O(A) molecule is not disordered but is situated at one position (identified as A) with an orientation that corresponds to one of the two found at high temperatures, whereas the solvate molecule associated with the bottom Fe_3O-(B) molecule is disordered in two positions just as found in the monoclinic phase. The occupancy ratio of these two disorder elements, group of Cl(4C) in position A (solid lines) and group of Cl(4B) in position B (open lines), at 169 K was found to be 30/70. Finally, as the temperature of the crystal is decreased to 122 K there is no disorder found in the solvate molecules (Figure 5). However, the solvate molecules associated with the two different Fe_3O molecules are in different positions. As shown in Figure 5, the solvate molecule of the top Fe_3O(A) molecule is at position A, while that of the bottom Fe_3O(B) molecule is at position B. With the variations of the relative positions between Fe_3O molecule and solvate molecule, the crystallographic phase transition at ~200 K can be readily monitored for complex **1**.

In the triclinic phase, the lattice packing arrangement at both 169 and 122 K has retained the layer structure found in the monoclinic high-temperature phase. In Figure 3b is given a stereoview of the packing arrangement of complex **1** at 169 K.

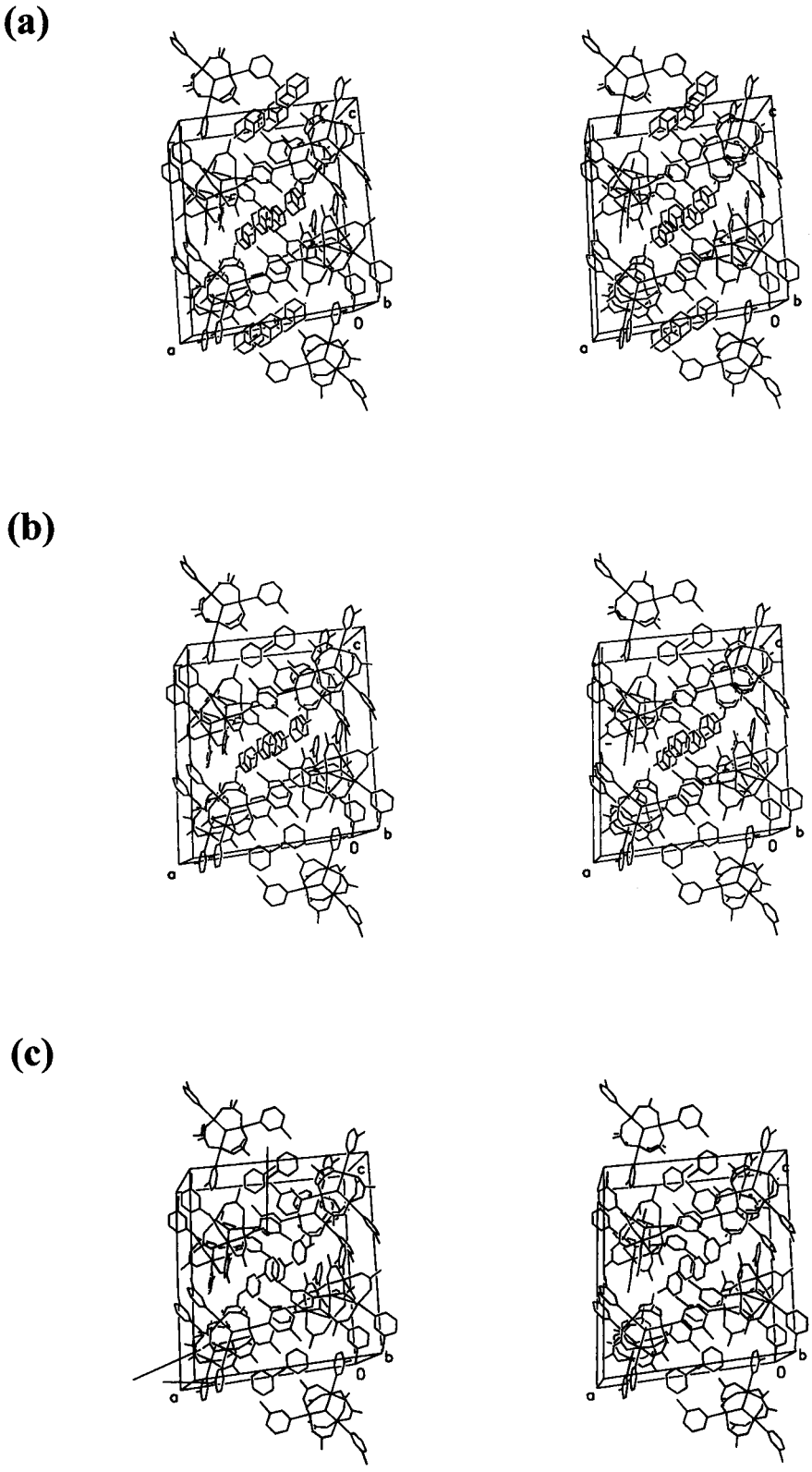

Figure 3. Stereoscopic views of the packing arrangement in the crystal of $[Fe_3O(O_2CCH_3)_6(3\text{-Cl-py})_3]\cdot 3\text{-Cl-py}$ (**1**). Plot a is for the monoclinic $P2_1/c$ crystal at 300 K. Plots b and c are for the triclinic $P\bar{1}$ crystal at 169 and 122 K, respectively.

The original Fe_3O(A) molecule (Figure 4) is located at the corner (*a*, *b*, 0) in the unit cell where the associated nondisordered 3-Cl-py solvate is right below the *ab* plane and the other Fe_3O-(B) molecule is at the corner (*a*, *b*, *c*) with the disordered solvate molecule located at the unit cell center. In Figure 3c it can be seen that the 122 K packing arrangement is similar to that at 169 K. Although the relative locations of the two different Fe_3O molecules in the unit cell have not changed as the temperature is decreased from 169 to 122 K, the disordered solvate molecule at the center of unit cell has become ordered in a preferred position (B) at 122 K. At this low temperature the crystal lattice of complex **1** adjusts all solvate molecules to statically ordered positions. Two conclusions can be made at this point. First, there are probably two phase transitions, one at ~200 K involving the monoclinic−triclinic structural phase transition. There is a second phase transition between 169 and 122 K

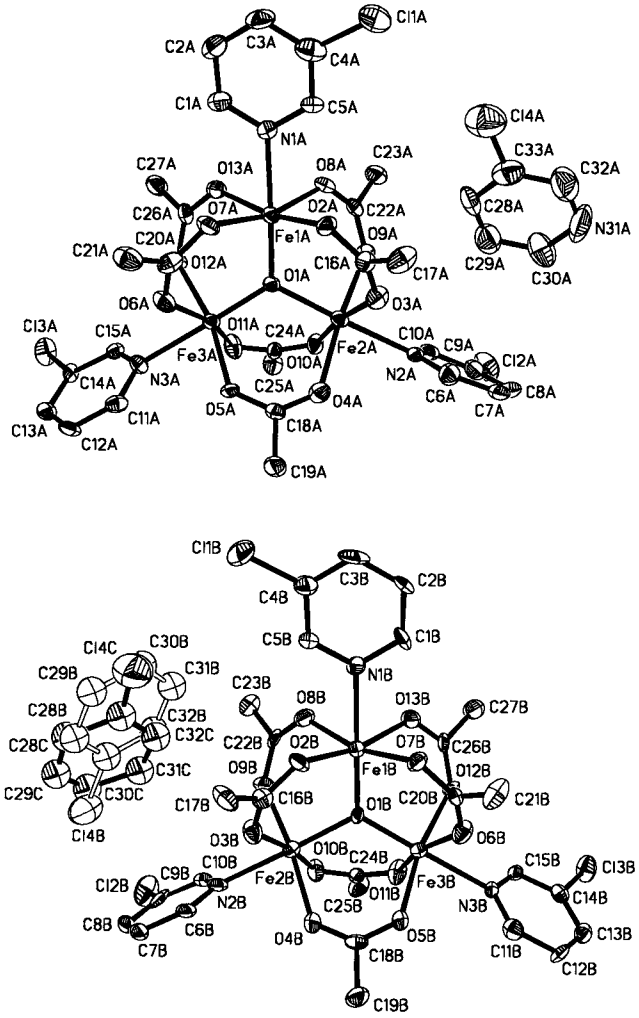

Figure 4. ORTEP plots of the molecular structures of the two crystallographically different μ_3-oxo-bridged trinuclear complexes accompanied by the solvate molecule in $[Fe_3O(O_2CCH_3)_6(3\text{-Cl-py})_3]\cdot 3\text{-Cl-py}$ (**1**) at 169 K. Atoms are shown as 50% equiprobability ellipsoids.

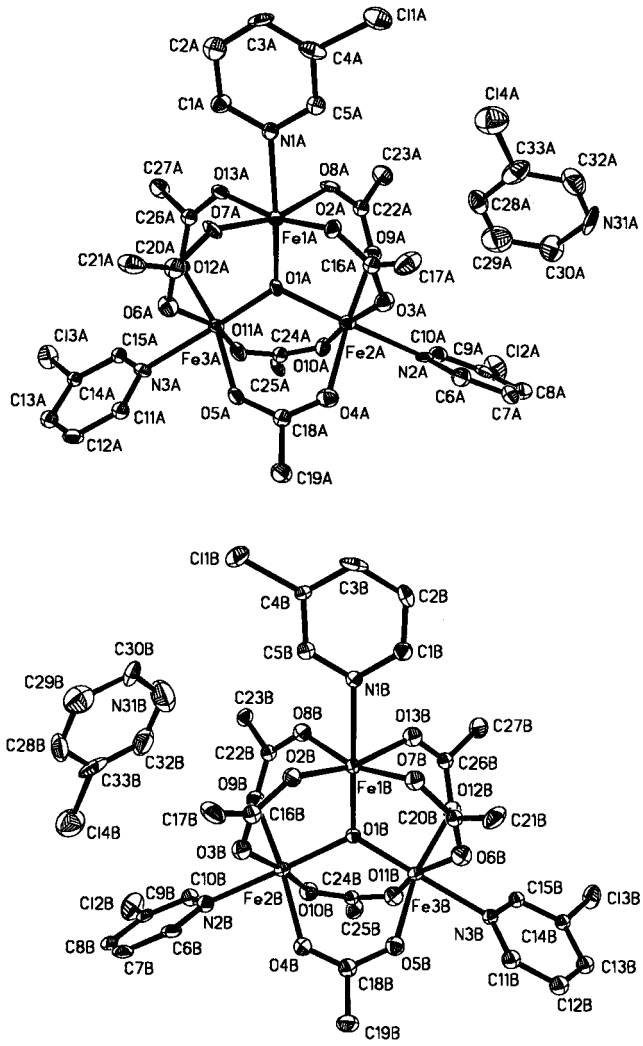

Figure 5. ORTEP plots of the molecular structures of the two crystallographically different μ_3-oxo-bridged trinuclear complexes accompanied by the solvate molecule in $[Fe_3O(O_2CCH_3)_6(3\text{-Cl-py})_3]\cdot 3\text{-Cl-py}$ (**1**) at 122 K. Atoms are shown as 50% equiprobability ellipsoids.

involving differences in the ordering and disordering of the solvate molecules. The second conclusion is that the solvate molecules are probably converting from being static at low temperatures to dynamically interconverting between sites at higher temperatures. The disappearance of the disordered structure for solvate molecules at low temperatures strongly suggests that the solvate molecules are not always static in the crystal lattice; at some elevated temperatures, when there is sufficient thermal energy, the solvate molecules start to move between two positions and as a result become dynamically disordered in the positions found in the crystal structures.

From the structure results that have been discussed, mechanisms for the phase transitions can be proposed. In the low-temperature triclinic phase at 122 K, the 3-Cl-py solvate molecules associated with two different Fe_3O(A) and Fe_3O(B) complexes are ordered and statically situated either at position A (solid lines) or at position B (open lines) as shown in Figure 3c. As the temperature of the crystal is increased, the solvate molecule at position B becomes disordered in two positions (A and B) and the crystal assumes the second phase shown in Figure 3b at 169 K. When the temperature is further increased to approach 200 K right below the phase transition, both of the solvate molecules originally at positions A and B have become disordered having very similar occupancy ratios of two disordered elements, and as a result, the relative positions of the two different Fe_3O complexes and their associated solvate molecules are very similar. As soon as the temperature reaches 200 K, the occupancy ratio of disordered elements for all solvate 3-Cl-py molecules become identical and so do the relative positions of the Fe_3O complexes and solvate molecules throughout the crystal lattice of complex **1** (Figure 3a). Thus, there is only one Fe_3O complex associated with one disordered 3-Cl-py molecule, where a pair of mirror images for the disordered solvate molecule are shown for the high-temperature monoclinic phase ($\geq$200 K).

The core structures of the Fe_3O complexes at 169 and 122 K have dimensions that indicate complex **1** is valence-trapped with very distinct dimensional differences between Fe^{III} and Fe^{II} ions. For both of the different Fe_3O(A) and Fe_3O(B) molecular units, the Fe−O bond distances to the central oxide ion clearly indicate that the Fe(2A) and Fe(2B) ions are the high-spin Fe^{II} ions in the complex: Fe(2A)−O(1A) = 2.007(5) Å and Fe(2B)−O(1B) = 1.990(5) Å at 169 K, and Fe(2A)−O(1A) = 2.043(6) Å and Fe(2B)−O(1B) = 2.020(1) Å at 122 K. Furthermore, a comparison of average distances for all six bonds about a given iron ion also indicates the Fe(2A) and Fe(2B) ions are the high-spin Fe^{II} ions in the complex **1**; see Table 4.

The temperature dependences of the Fe−O(center oxide) bond lengths for $[Fe_3O(O_2CCH_3)_6(3\text{-Cl-py})_3]\cdot 3\text{-Cl-py}$ (**1**) in both the monoclinic ($\leq$200 K) and the triclinic ($\leq$200 K) crystal systems are plotted in Figure 6. The Fe−O(oxide) bond lengths clearly

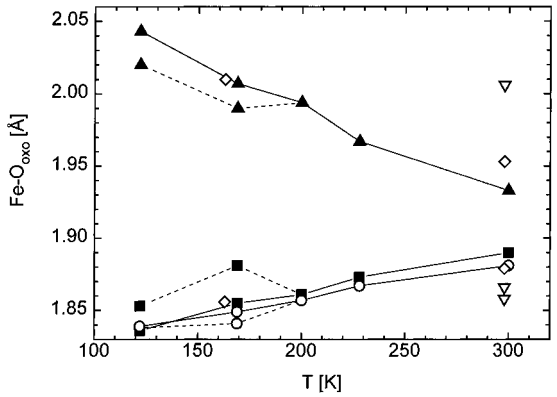

Figure 6. Temperature dependence of Fe−O(oxide) bond lengths for $[Fe_3O(O_2CCH_3)_6(3\text{-Cl-py})_3]\cdot 3\text{-Cl-py}$ (**1**) in the monoclinic (≥200 K) and the triclinic (<200 K) crystal systems. Data connected by solid lines are shown for bond lengths of (○) Fe_1-O, (▲) Fe_2-O, and (■) Fe_3-O, whereas data linked by dashed lines are for Fe(1A)−O, Fe(2A)−O, and Fe(3A)−O. The Fe−O bond lengths (◇) for $[Fe_3O(O_2CCH_3)_6(4\text{-Et-py})_3]\cdot 4\text{-Et-py}$ at 298 and 163 K are also shown for comparison. Solid lines or dashed lines connecting data points for one type of Fe−O bond length are drawn to guide the eyes only.

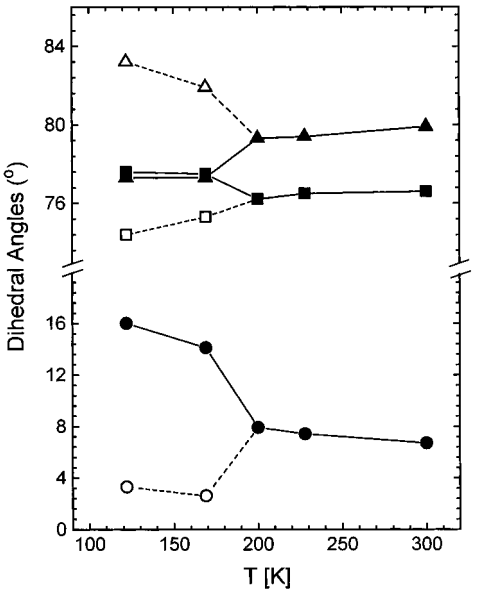

Figure 7. Temperature dependence of dihedral angles between the 3-Cl-py ligand plane and the Fe_3O plane for $[Fe_3O(O_2CCH_3)_6(3\text{-Cl-py})_3]\cdot 3\text{-Cl-py}$ (**1**) in the monoclinic and triclinic crystal systems. The data consisting of solid symbols connected by solid lines represent the dihedral angles of (●) $Fe_3O(A)-L_1$, (▲) $Fe_3O(A)-L_2$, and (■) $Fe_3O(A)-L_3$, whereas the data consisting of open symbols at low temperatures linked by dashed lines are for $Fe_3O(B)-L_1$, $Fe_3O(B)-L_2$, and $Fe_3O(B)-L_3$. The solid lines or dashed lines connecting data points for one type of Fe−O bond length are drawn to guide the eyes only.

show that complex **1** is becoming more and more valence-trapped when the temperature is decreased. Due to the structure similarity in pyridine ligand orientations to complex **1**, bond length data for the 4-Et-py complex (◇) at room temperature (nearly valence-detrapped) and 163 K (valence-trapped) are shown for comparison. In spite of the phase transition at ∼200 K splitting the bond length data for complex **1** at low temperatures, the high-spin Fe^{II} (△) and high-spin Fe^{III} (○ and □) ions are still distinguishable. For the two different Fe_3O-(A) and Fe_3O(B) molecules at 169 and 122 K, the Fe−O(oxide) bond length data are connected by different lines in Figure 6: solid lines for the Fe_3O(A) molecule associated with the solvate molecule in position A at both temperatures and dashed lines for the Fe_3O(B) molecule with a *non*-disordered solvate at 122 K in position B (Figure 5) or a disordered solvate molecule at 169 K (Figure 4).

There are two additional observations that can be made regarding the bond length data for the two different Fe_3O molecules (Figure 6). First, the Fe−O(oxide) bond lengths of these two Fe_3O molecules are becoming more equivalent when the temperature is decreased from 169 to 122 K, suggesting the valence distributions (Fe^{II} and Fe^{III}) in the two Fe_3O molecules are becoming identical and very close to a completely valence-trapped state at 122 K. The other observation is that the bond length differences between the Fe^{II} (▲) and Fe^{III} (■) ions at 169 K for the Fe_3O(B) molecule with the disordered solvate of position B (dash line) are much less than those for the Fe_3O(A) molecule which has a *non*-disordered solvate at position A (solid line). This indicates that the structure of the Fe_3O(B) molecule is more valence-detrapped than the other crystallographically distinct molecule. This also suggests that the disordered nature of the solvate molecule impacts on the valence-detrapping in complex **1**. In fact, this is the first case wherein distinctions of valence structures found in two chemically equivalent mixed-valence Fe_3O molecules can be associated with the structure difference of neighboring ordered or disordered solvate molecules in a crystal lattice.

In Figure 7 is shown the temperature dependence of dihedral angles between 3-Cl-py ligand plane and the Fe_3O plane for complex **1**. Above the higher temperature phase transition temperature (≥200 K), the variations of all three dihedral angles are almost linear with the temperature changes. When the temperature is below 200 K, the data for each of three dihedral angles are split into two data sets (solid and open symbols) due to the two crystallographically different Fe_3O molecules in the triclinic unit cell. At low temperatures the filled symbols are for the Fe_3O(A) molecule associated with the solvate molecule at position A and open-symbol data are for the Fe_3O(B) molecule with a solvate molecule in position B (Figures 4 and 5). For the Fe_3O(A) molecule, the dihedral angles $Fe_3O(A)-L_2$ (▲) and $Fe_3O(A)-L_3$ (■) are almost identical at low temperatures, whereas the $Fe_3O(A)-L_1$ (●) angle increases as the temperature is decreased. In contrast, for the Fe_3O(B) molecule (open symbols), the difference between dihedral angles $Fe_3O(B)-L_2$ (△) and $Fe_3O(B)-L_3$ (□) and the $Fe_3O(B)-L_1$ (○) angle decreases as the temperature is decreased. All these differences of variations on dihedral angles in the two unique molecules in the triclinic unit cell indicate that there are some necessary structure adjustments in the Fe_3O complex in order to couple with changes in the solvate molecule at the different positions (A or B). In Figure 8, the relatively large difference (∼12°) between the $Fe_3O(A)-L_1$ (●) and $Fe_3O(B)-L_1$ (○) dihedral angles for the unique 3-Cl-py ligand that is nearly parallel to the Fe_3O plane shows that the orientation of this ligand ring is sensitive to the structural changes of the neighboring solvate molecule, which is due to the very short distance between the Cl(1A) or Cl(1B) atoms and the 3-Cl-py solvate. A coupled motion of solvate molecules and 3-Cl-py ligands is likely.

^{57}Fe Mössbauer Spectroscopy. Variable-temperature Mössbauer spectra were collected for $[Fe_3O(O_2CCH_3)_6(3\text{-Cl-py})_3]\cdot 3\text{-Cl-py}$ (**1**). It is shown that complex **1** is valence-trapped at 110 K and becomes detrapped at room temperature as determined by the ^{57}Fe Mössbauer technique. In addition, an unusual splitting of the resonance lines for the high-spin Fe^{II} signal into two doublets is observed in the variable-temperature Mössbauer spectra.

In Figure 8 are shown some Mössbauer spectra for complex **1** taken in the range 110−293 K. All spectra were least-squares-fit to Lorentzian line shapes. At the highest temperature (293

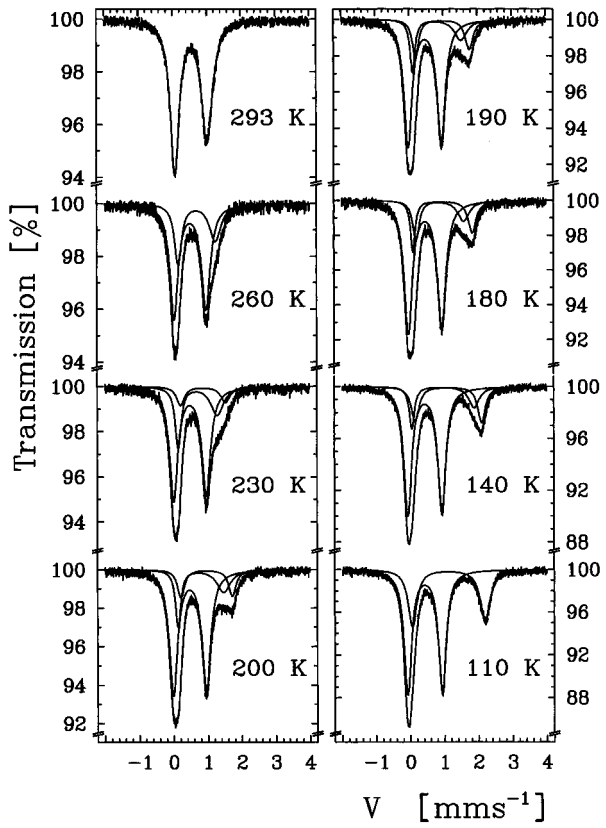

Figure 8. Variable-temperature ^{57}Fe Mössbauer spectra for $[Fe_3O(O_2CCH_3)_6(3\text{-Cl-py})_3]\cdot 3\text{-Cl-py}$ (**1**) with the fitting results of model a.

K) the spectrum was fit to a single doublet, showing that complex **1** is valence-detrapped on the Mössbauer time scale. In contrast, the spectrum at 110 K can be definitively fit with two doublets, where the more intense doublet corresponds to the two high-spin Fe^{III} ions and the less intense doublet is for the one high-spin Fe^{II} ion in each Fe_3O complex; complex **1** is valence-trapped at 110 K. However, fitting the spectra at intermediate temperatures is not straightforward. An attempt to fit spectra in the 140−230 K range with just two doublets was not successful due to a distinct line splitting observed in the high-velocity component of the Fe^{II} doublet. In order to accommodate this unusual component of the Fe^{II} signal, it is necessary to introduce an additional doublet to fit the spectra. By the addition of one more Fe^{II} doublet, each spectrum was fit with three different doublets. Initially it was found that constraining the two Fe^{II} doublets to equal areas failed to satisfactorily fit the spectra at most temperatures. After the constraints on the peak area parameters for the two Fe^{II} doublets were removed, least-squares fits converged to give four different fitting models, each with three doublets.

In Figure 9 are given the fitting results for the 200 K spectrum obtained from the four different three-doublet models. In models a and b, the fitting process was initiated with a fixed parameter of quadrupole splitting (ΔE_Q) for the two Fe^{II} doublets (Fe^{II}_a and Fe^{II}_b), each with different center shifts (δ). In models c and d, the fitting was initiated with a fixed center shift parameter for the two Fe^{II} doublets, each with different quadrupole splittings. All four models satisfactorily explain the line shapes of the Mössbauer spectra in the 140−230 K range. The fits corresponding to model a are shown in Figure 8. The final fitting parameters for these four models are listed in Table 6. In the temperature range 140−230 K the fitting parameters for the two high-velocity fitting lines accounting for the split Fe^{II} signal are almost the same for all four models, suggesting a higher certainty for fitting this portion of the spectrum. As

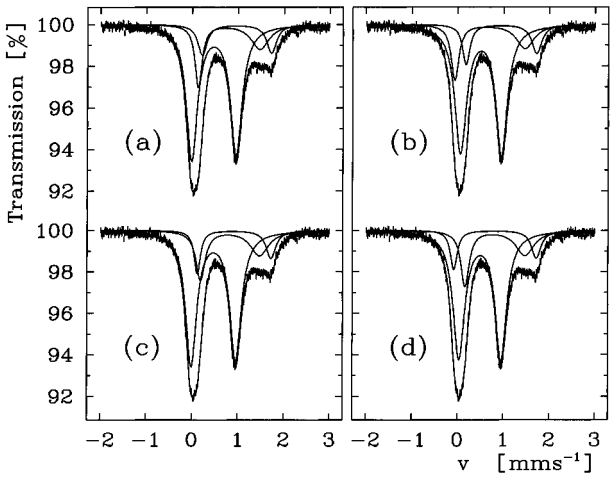

Figure 9. Four possible models of one Fe^{III} and two Fe^{II} doublets with different fitting parameters of center shift and quadrupole splitting for the 200 K ^{57}Fe Mössbauer spectrum of $[Fe_3O(O_2CCH_3)_6(3\text{-Cl-py})_3]\cdot 3\text{-Cl-py}$ (**1**).

shown in Figure 8 for model a, the separation (∼0.26 mm s^{-1}) between the two high-velocity Fe^{II} fitting lines in the spectra is almost temperature independent, whereas the relative intensities of these two fitting lines interchange as the temperature is varied, and the positions of both lines move toward the center of spectrum (zero velocity) with increasing temperature. As the temperature is increased to 260 K, the Fe^{II} and Fe^{III} signals become appreciably overlapped in the spectrum and the experimental spectrum can be fit to two doublets with an intensity area ratio close to 2/1.

In Figure 10 are shown the temperature dependencies of the center shift (top, uncorrected for second-order Doppler shift) and quadrupole splitting (bottom) for each of the doublets in the Mössbauer spectra of complex **1**, where the data in the range 140−230 K are taken from the fitting model a. For comparison, center shift data reported[4f] for the Fe^{II} ion in $[Cr^{III}_2Fe^{II}O(O_2CCH_3)_6(py)_3]\cdot py$ (●) and for the Fe^{III} ion in $[Fe^{III}2Co^{II}O(O_2CCH_3)_6(py)_3]\cdot py$ (○) are also plotted. It is clear that at 110 K complex **1** is valence-trapped on the Mössbauer time scale.

Although all of the four fitting models are equally effective in reproducing the line shapes of the spectra from 140 to 230 K, models b and d are not appropriate because the parameters (center shift and quadrupole splitting) are not reasonable. In model b, the quadrupole splitting parameters for the two Fe^{II} doublets are almost identical, whereas the differences between the center shift parameters for the two doublets are the largest (∼0.24 mm s^{-1}) among all models (Table 6). In contrast, in model d, the center shift parameters for the two Fe^{II} doublets are almost identical, whereas the differences between the quadrupole splitting parameters for the two doublets are the largest (∼0.48 mm s^{-1}) among all models (Table 6). In ^{57}Fe Mössbauer spectroscopy, since the center shift parameters reflect the valence of an iron ion and the quadrupole splitting energy indicates the coordination symmetry about the ion, it would be very difficult to rationalize that within a small temperature region (110−140 K) the Fe^{II} ion is abruptly converted into two ions with very different valences but identical coordination symmetries (model b) or with identical oxidation states but different symmetries (model d). Similar abrupt changes in parameters are also found from 230 to 260 K, where the two Fe^{II} ions converge to one Fe^{II} ion in both model b (center shift) and model d (quadrupole splitting). Such unusual and abrupt changes in Mössbauer parameters have never been reported for any Fe_3O complexes. Furthermore, the results from the X-ray structures do not support models b and d.

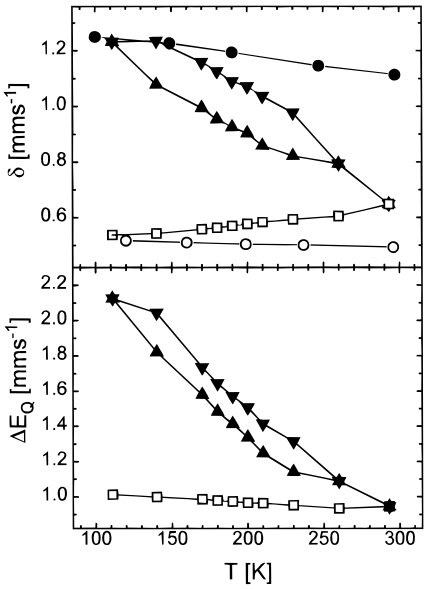

Figure 10. Top: Plots of the center shift (δ) relative to α-iron (at room temperature) versus temperature for "Fe^{II}" (filled symbols) and "Fe^{III}" (open symbols) doublets in the Mössbauer spectrum of $[Fe_3O(O_2CCH_3)_6(3\text{-Cl-py})_3]\cdot 3\text{-Cl-py}$: ▼, ▲, and □ from the fitting model a. Other plots: $[Cr^{III}_2Fe^{II}O(O_2CCH_3)_6(py)_3]\cdot py$ (●); $[Fe^{III}_2Co^{II}O(O_2CCH_3)_6(py)_3]\cdot py$ (○). Bottom: Plots of quadrupole splitting (ΔE_Q) versus temperature for "Fe^{II}_a" (▼), "Fe^{II}_b" (▲), and "Fe^{III}" (□) doublets in the spectra of $[Fe_3O(O_2CCH_3)_6(3\text{-Cl-py})_3]\cdot 3\text{-Cl-py}$ from the fitting model a. Lines connecting the data points are drawn to guide the eyes only.

On the other hand, for models a and c, the fitting parameters for the Fe^{II}_a and Fe^{II}_b signals are in an intermediate range (∼0.08−0.16 mm s^{-1} for center shift and ∼0.17−0.32 mm s^{-1} for quadrupole splitting). At temperatures below the structural phase transition temperature (∼200 K), the fitting results for the two different Fe^{II} ions in models a and c agree with the results of the crystal structures that show there are two valence-trapped Fe_3O molecules with similar Fe−O(oxide) bond lengths at 122 K and two Fe_3O molecules with different Fe−O bond lengths at 169 K (Figure 7). However, at first it seems that the fitting parameters of models a and c are not completely consistent with the results of the crystal structures at temperatures above the phase transition (∼200 K), where only one type of Fe^{II} ion is found. The differences in detecting two types of Fe^{II} ions using these two physical methods is likely due to the different time scales for each technique. Since the time scale for Mössbauer spectroscopy is much shorter than that of single-crystal X-ray structure determinations, it is not unreasonable that if there are some dynamics affecting the Fe^{II} ions in the crystal lattice, the ^{57}Fe Mössbauer technique would detect two Fe^{II} ions with slight differences in valence and structure symmetry, whereas in the X-ray structure only one average Fe^{II} ion is seen.

The valence-detrapping temperature of 293 K for complex **1** is similar to those (∼280−300 K) for all Fe_3O complexes that have the layer type of lattice packing. Lower detrapping temperatures (∼100−200 K) have been reported for Fe_3O complexes with "stacked" packing arrangements. In the absence of strong intermolecular interactions in the crystal lattice of complex **1**, it is understandable that the temperature range (∼200 deg) for the valence detrapping is larger than that for Fe_3O complexes with py···py intermolecular ligand overlaps (∼100 deg) or H-bonding (∼10 deg) between molecules. As shown in Figure 10 (model a), the variable-temperature center shift data for complex **1** show that the valence-averaging process of Fe^{III} and Fe^{II} ions starts at temperatures above 110 K and is not complete until room temperature.

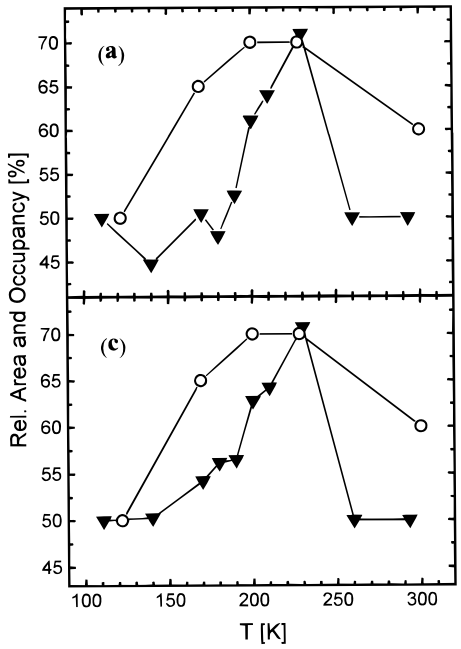

Figure 11. Temperature dependence of the area (%) for "Fe^{II}_a" doublets (▼) relative to the overall area of "Fe^{II}" ("Fe^{II}_a" and "Fe^{II}_b") doublets in the fitting models a and c for the ^{57}Fe Mössbauer spectra of $[Fe_3O(O_2CCH_3)_6(3\text{-Cl-py})_3]\cdot 3\text{-Cl-py}$ (**1**). The temperature dependence of the relative occupancy (%) for solvate molecules in position "A" (○) in the unit cell are also shown for comparison purposes. The latter data are from the X-ray structure refinements. Lines connecting data points are drawn to guide the eyes only.

There is no line broadening observed in all the fitting models of the Mössbauer spectra for complex **1**. As has been suggested in previous studies on several valence-detrapped Fe_3O complexes, the absence of line broadening observed in the Mössbauer spectra in the intermediate-temperature region is due to the fact that the rate of intramolecular electron transfer for a given Fe_3O molecule is not starting at some small value and increasing gradually with temperature until the rate goes through the "window" of the Mössbauer technique. In contrast, it is thought that at a given temperature some molecules are in a domain where the environment is more static and other Fe_3O molecules are in other domains where the environment is more dynamic. Domain walls are regions between the two types of domain. If the domain walls are moving about the crystal at a rate faster than the Mössbauer technique can sense, this could lead to the absence of line broadening due to a coalescence phenomenon. At a particular temperature in the intermediate region, a certain fraction of complexes are in "static" domains, while the other complexes are in "dynamic" domains. The net results for the fast movements of domain walls is that the Fe^{II} doublet picks up some character of the Fe^{III} doublet and *vice versa*. The two Mössbauer doublets move together, and eventually when all complexes are in dynamic domains, only a single average doublet is seen (Figure 10).

Effects of the Dynamically Disordered Solvate Molecules. The appearance of three doublets in the Mössbauer spectra at temperatures from 140 to 230 K indicates that there are two different types of Fe^{II} ions and one Fe^{III} ion trapped on the Mössbauer time scale. The presence of two types of Fe^{II} ions seems to agree with the presence of two different Fe_3O complexes in the triclinic unit cell at temperatures below 200 K. However, the relative area intensity of these two Fe^{II}_a and Fe^{II}_b signals in each Mössbauer spectrum is temperature dependent. In Figure 11 the relative area for the Fe^{II}_a doublet

Table 6. ^{57}Fe Mössbauer Fitting Parameters for $[Fe_3O(O_2CCH_3)_6(3\text{-Cl-py})_3]\cdot 3\text{-Cl-py}$[a]

	δ, mm/s[b]			ΔE_Q, mm/s			Γ, mm/s[c]			% area		
T, K	Fe^{III}	Fe^{av}	Fe^{II}	Fe^{III}	Fe^{av}	Fe^{II}	Fe^{III}	Fe^{av}	Fe^{II}	Fe^{III}	Fe^{av}	Fe^{II}
110	0.537(1)		1.232(3)	1.012(2)		2.125(6)	3.132(2) 0.136(2)		3.151(5) 0.171(5)	65.1(6)		34.9(6)
260	0.609(6)		0.807(17)	0.934(5)		1.088(19)	0.143(5) 0.156(9)		0.126(12) 0.203(25)	68.2(65)		31.8(65)
293		0.648(2)			0.945(3)			0.153(3) 0.193(3)			100	

Model a

	δ, mm/s[b]			ΔE_Q, mm/s			Γ, mm/s[c]			% area		
T, K	Fe^{III}	Fe^{II}_a	Fe^{II}_b	Fe^{III}	Fe^{II}_a	Fe^{II}_b	Fe^{III}	Fe^{II}_a	Fe^{II}_b	Fe^{III}	Fe^{II}_a	Fe^{II}_b
140 18	0.543(1)	1.078(15)	1.235(10)	0.998(2)	1.820(23)	2.044(10)	0.136(2) 0.140(2)	0.091(11) 0.182(24)	0.136(9) 0.132(13)	66.7(7)	14.9(36)	18.4(33)
170	0.558(1)	0.994(18)	1.159(12)	0.986(3)	1.579(27)	1.736(11)	0.140(2) 0.146(3)	0.088(11) 0.201(32)	0.122(10) 0.138(19)	67.1(11)	16.6(45)	16.3(39)
180	0.563(2)	0.954(20)	1.126(13)	0.978(3)	1.483(31)	1.645(12)	0.143(3) 0.151(3)	0.081(13) 0.201(42)	0.114(10) 0.139(21)	68.3(14)	15.2(49)	16.5(41)
190	0.570(2)	0.925(22)	1.090(13)	0.973(3)	1.413(35)	1.572(12)	0.144(3) 0.148(3)	0.087(14) 0.223(44)	0.113(10) 0.139(23)	67.1(16)	17.3(59)	15.6(48)
200	0.577(2)	0.903(22)	1.072(15)	0.965(3)	1.336(34)	1.507(17)	0.145(3) 0.151(4)	0.093(15) 0.236(47)	0.121(16) 0.129(28)	67.1(23)	20.1(64)	12.8(47)
210	0.583(3)	0.859(27)	1.037(23)	0.963(4)	1.247(43)	1.414(21)	0.162(4) 0.151(6)	0.099(19) 0.259(54)	0.128(19) 0.153(42)	64.7(34)	22.6(86)	12.7(65)
230	0.593(5)	0.822(27)	0.977(43)	0.952(5)	1.141(40)	1.314(48)	0.144(5) 0.152(9)	0.104(28) 0.221(72)	0.136(42) 0.161(77)	64.5(64)	25.2(153)	10.3(105)

Model b

	δ, mm/s[b]			ΔE_Q, mm/s			Γ, mm/s[c]			% area		
T, K	Fe^{III}	Fe^{II}_a	Fe^{II}_b	Fe^{III}	Fe^{II}_a	Fe^{II}_b	Fe^{III}	Fe^{II}_a	Fe^{II}_b	Fe^{III}	Fe^{II}_a	Fe^{II}_b
140	0.570(5)	0.999(17)	1.225(9)	0.943(9)	2.001(23)	1.974(9)	0.150(4) 0.140(2)	0.097(8) 0.195(24)	0.125(9) 0.129(15)	66.3(8)	16.7(40)	17.0(36)
170	0.592(6)	0.901(18)	1.145(9)	0.920(13)	1.773(26)	1.767(10)	0.155(4) 0.146(3)	0.092(9) 0.208(31)	0.106(9) 0.138(19)	66.7(11)	17.4(44)	15.9(38)
180	0.601(8)	0.872(22)	1.115(10)	0.903(16)	1.695(32)	1.684(12)	0.158(4) 0.150(3)	0.094(11) 0.225(36)	0.102911) 0.129(24)	67.4(15)	18.9(53)	13.7(44)
190	0.605(8)	0.836(24)	1.077(10)	0.902(17)	1.606(33)	1.605(11)	0.155(4) 0.148(3)	0.100(11) 0.273(39)	0.099(11) 0.137(24)	66.3(16)	19.1(58)	14.6(48)
200	0.614(8)	0.805(22)	1.054(11)	0.893(16)	1.528(31)	1.539(12)	0.155(4) 0.151(4)	0.102(12) 0.234(44)	0.097(11) 0.133(26)	67.2(21)	19.5(59)	13.4(45)
210	0.621(9)	0.763(30)	1.015(17)	0.884(19)	1.420(46)	1.445(19)	0.152(6) 0.151(5)	0.115(13) 0.267(48)	0.108(15) 0.157(39)	64.0(31)	22.7(76)	13.4(61)
230	0.627(13)	0.723(26)	0.958(30)	0.889(29)	1.331(31)	1.329(31)	0.148(6) 0.156(7)	0.105(23) 0.183(69)	0.100(18) 0.173(48)	68.1(47)	18.1(117)	13.9(86)

Model c

	δ, mm/s[b]			ΔE_Q, mm/s			Γ, mm/s[c]			% area		
T, K	Fe^{III}	Fe^{II}_a	Fe^{II}_b	Fe^{III}	Fe^{II}_a	Fe^{II}_b	Fe^{III}	Fe^{II}_a	Fe^{II}_b	Fe^{III}	Fe^{II}_a	Fe^{II}_b
140	0.543(1)	1.191(4)	1.135(9)	0.998(3)	1.734(43)	2.044(15)	0.136(2) 0.140(2)	0.136(11) 0.190(24)	0.095(10) 0.125(15)	66.6(8)	16.8(40)	16.6(36)
170	0.558(1)	1.116(5)	1.040(10)	0.986(3)	1.507(47)	1.829(18)	0.140(3) 0.146(3)	0.122(11) 0.207(32)	0.085(10) 0.134(20)	67.0(12)	17.9(48)	15.1(41)
180	0.563(2)	1.083(6)	1.006(12)	0.978(3)	1.415(54)	1.746(19)	0.149(3) 0.150(3)	0.117(12) 0.217(40)	0.079(11) 0.128(23)	67.9(15)	18.1(54)	14.1(44)
190	0.570(2)	1.047(6)	0.968(13)	0.974(3)	1.346(57)	1.667(20)	0.143(3) 0.148(3)	0.116(11) 0.229(41)	0.082(10) 0.134(25)	66.8(17)	18.7(61)	14.4(49)
200	0.577(2)	1.025(7)	0.935(14)	0.966(3)	1.281(57)	1.602(21)	0.145(3) 0.151(4)	0.121(12) 0.240(47)	0.082(12) 0.127(29)	66.9(24)	20.8(66)	12.3(49)
210	0.582(3)	0.981(11)	0.888(21)	0.963(4)	1.182(21)	1.520(31)	0.146(4) 0.151(6)	0.129(14) 0.265(55)	0.084(16) 0.152(44)	64.2(35)	23.0(90)	12.8(67)
230	0.592(5)	0.927(20)	0.837(22)	0.954(6)	1.097(22)	1.405(64)	0.145(5) 0.151(9)	0.121(15) 0.224(66)	0.087(27) 0.160(72)	64.1(61)	25.4(142)	10.5(98)

Model d

	δ, mm/s[b]			ΔE_Q, mm/s			Γ, mm/s[c]			% area		
T, K	Fe^{III}	Fe^{II}_a	Fe^{II}_b	Fe^{III}	Fe^{II}_a	Fe^{II}_b	Fe^{III}	Fe^{II}_a	Fe^{II}_b	Fe^{III}	Fe^{II}_a	Fe^{II}_b
140	0.572(5)	1.117(10)	1.105(4)	0.940(10)	1.751(38)	2.209(15)	0.150(4) 0.140(2)	0.123(11) 0.189(25)	0.098(7) 0.132(14)	66.4(8)	15.7(39)	18.0(35)
170	0.589(7)	1.024(12)	1.021(5)	0.925(13)	1.532(39)	2.017(17)	0.155(4) 0.146(3)	0.109(10) 0.209(31)	0.089(9) 0.137(19)	66.7(11)	17.6(45)	15.6(39)

Table 6 (Continued)

	Model d											
	δ, mm/s[b]			ΔE_Q, mm/s			Γ, mm/s[c]			% area		
T, K	Fe^{III}	Fe^{II}_a	Fe^{II}_b	Fe^{III}	Fe^{II}_a	Fe^{II}_b	Fe^{III}	Fe^{II}_a	Fe^{II}_b	Fe^{III}	Fe^{II}_a	Fe^{II}_b
180	0.597(8)	0.984(15)	0.985(6)	0.911(15)	1.428(47)	1.927(19)	0.158(4) 0.151(3)	0.105(13) 0.209(44)	0.090(10) 0.141(22)	67.8(15)	15.8(54)	16.4(44)
190	0.598(8)	0.955(16)	0.954(5)	0.918(15)	1.377(48)	1.853(19)	0.154(4) 0.148(3)	0.106(11) 0.239(37)	0.093(11) 0.135(24)	66.2(16)	19.5(57)	14.2(47)
200	0.602(7)	0.926(15)	0.928(6)	0.916(14)	1.303(44)	1.798(20)	0.153(4) 0.151(4)	0.108(11) 0.241(40)	0.089(12) 0.126(26)	66.9(21)	20.9(56)	12.1(42)
210	0.606(9)	0.882(21)	0.889(9)	0.916(18)	1.211(57)	1.714(34)	0.150(5)	0.119(13)	0.101(17)	64.2(31)	23.9(75)	11.9(57)

[a] Peaks were least-squares-fit to Lorentzian line shapes with equal areas for both components of a doublet; errors in the last significant figure are given in parentheses. [b] Center shifts relative to iron metal at room temperature. [c] Half-width at half-maximum listed in order of increasing velocity of the peak.

(▽) in either of the two models a and c is shown plotted as a function of temperature (the sum of relative areas for the Fe^{II}_a and Fe^{III}_b doublets is always 100%). The data for model a given in the top of Figure 11 show that there is 50% Fe^{II}_a doublet at 122 K, but the relative area of this doublet increases to >70% at 230 K, whereupon it decreases to 50% at 300 K. This suggests that these two Fe^{II} signals in the Mössbauer spectra do not simply correspond to the two crystallographically different Fe_3O molecules of equivalent occupancy in the crystal structures. The origin of the two Fe^{II} doublets lies in the nature (ordered or disordered) of the solvate molecules. Figure 11 also shows the temperature dependence for the relative occupancy of the solvate molecules located in position A (○) versus the overall occupancy of all solvate molecules in both positions A and B in the unit cell as determined in the X-ray structure refinements. From the comparison of the two data sets shown in Figure 11, it is clear that near the phase transition temperature (~200 K) there is an increase in the magnitude for both the relative area intensity of the Fe^{II}_a signal in Mössbauer spectra and the relative occupancy of the solvate molecules in position A in the crystal structure. This strongly suggests the two Fe^{II} signals in Mössbauer spectra can be attributed to the different positions of neighboring solvate molecules relative to each Fe_3O complex in the lattice. In order to match the dynamic order−disorder transformation as well as the alternating dipole moments of the solvate molecules in the crystal lattice, the orientations of 3-Cl-py ligands and the symmetry of the whole Fe_3O molecule must be dynamically adjusted to give an energetically favorable structure. Thus, whenever a given solvate molecule moves to position A or B, a corresponding change in structure of Fe_3O molecule leads to an Fe^{II}_a or Fe^{II}_b signal, respectively, appearing in the Mössbauer spectrum.

From the results of the variable-temperature Mössbauer spectra and the X-ray structures of complex **1**, it is suggested that, in addition to influencing the structural phase transition, the solvate molecules also have significant effects on the valence-detrapping process and indirectly the rates of intramolecular electron transfer. On the basis of the results from the crystal structure and Mössbauer studies, the process of valence detrapping in $[Fe_3O(O_2CCH_3)_6(3\text{-Cl-py})_3]\cdot$3-Cl-py (**1**) from 110 K to room temperature can be divided into four different temperature ranges, as summarized in the following discussion.

First, at low temperatures (≤~120 K) each of the two types of Fe_3O molecules is associated with a solvate molecule in a fixed position (A or B). The Mössbauer signal is characteristic of a trapped-valence Fe_3O complex. The two crystallographically different complexes are structurally very similar, and the Mössbauer technique cannot distinguish between them. The crystal lattice is quite compact, and there is no room for motion of either 3-Cl-py solvate or ligand molecules.

As the temperature of the crystal is increased to the range ~140−180 K, the packing of the crystal lattice becomes less tight and some solvate molecules located in position B and associated with the Fe_3O(B) molecule start to become dynamically disordered between two positions (A and B). The Fe_3O complexes near these solvate molecules may also have "extra room" so that a 3-Cl-py ligand can librate. Because of the greater sensitivity in the Mössbauer response to environmental changes for the high-spin Fe^{II} ions compared to the high-spin Fe^{III} ions, two types of Fe^{II} Mössbauer signals having nearly equivalent intensities are seen in the Mössbauer spectra in this temperature range (Figure 8). The process of valence averaging also sets in at ~140 K. As can be seen in Figure 10, it is at this temperature that the center shifts for two Fe^{II} doublets and one Fe^{III} doublet (▼, ▲, and □) start deviating from the data for the Fe^{II} ion in $[Cr^{III}_2Fe^{II}O(O_2CCH_3)_6(py)_3]\cdot$py (●) and the Fe^{III} ion in $[Fe^{III}_2Co^{II}O(O_2CCH_3)_6(py)_3]\cdot$py (○). Clearly, in this temperature range (~140−180 K), half of the solvate molecules have become dynamic. This tends to change the potential-energy surface for the nearby Fe_3O complexes such that there are now three minima at about the same energy. Half of the Fe_3O complexes suddenly are able to tunnel between the three different states. Intramolecular electron transfer occurs in these complexes at a faster rate than the $\sim 10^9$ s^{-1} rate that the ^{57}Fe Mössbauer technique can sense. There is no evidence in the Mössbauer spectra of line broadening. Thus, the rate of intramolecular electron transfer does not increase from some low value to eventually go through the ^{57}Fe Mössbauer window of $\sim 10^7-10^9$ s^{-1}.

When complex **1** is near the temperature for the structural phase transition (~190−230 K), there is more thermal energy for additional molecules (solvate and Fe_3O complexes) to become dynamic. Within this temperature range, all of the solvate molecules originally sitting statically in either position A or B have become dynamically disordered between both positions. In the ~190−230 K range, the relative intensity of the two Fe^{II} Mössbauer signals varies considerably. This difference may be due to either different amounts of Fe_3O complexes in the two different sites or differences in recoilless fractions due to differences in the two Fe_3O sites. It is interesting that two different Fe^{II} signals are seen above ~200 K, where the X-ray structures indicate the crystal is monoclinic and there is only one type of Fe_3O complex. There are no discontinuities in the Mössbauer parameters seen in this temperature range. Therefore, the valence-detrapping process does not seem to be precipitiously affected by the phase transition. Thus, the parameters for the two Fe^{II} doublets and the one Fe^{III} doublet change smoothly to become those of the average signal at 300 K (Figure 10).

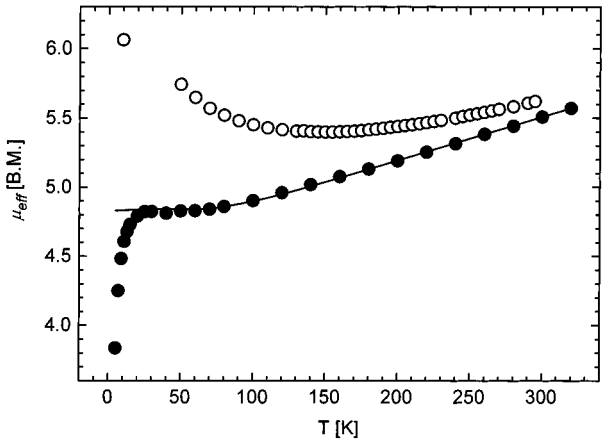

Figure 12. Effective magnetic moment versus temperature for a powder (●) and a single-crystal (○) sample with the *b* axis parallel to the magnetic field for $[Fe_3O(O_2CCH_3)_6(3\text{-Cl-py})_3]\cdot 3\text{-Cl-py}$ (**1**). The solid line represents the theoretical fit to the HDVV model with $S_1 = S_3 = {}^5/_2$ and $S_2 = 2$ and with $J = -11.5$ cm^{-1}, $J' = -83.5$ cm^{-1}, and $g = 2.00$.

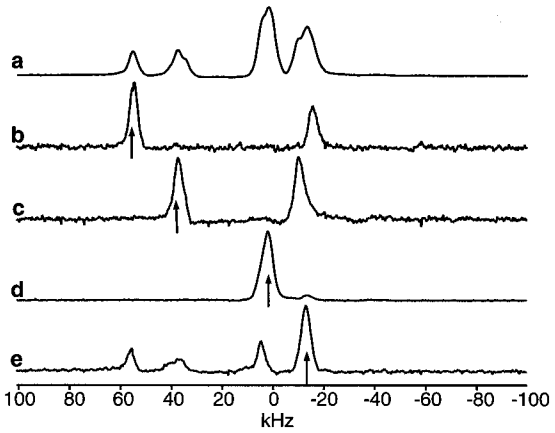

Figure 13. ^{2}H NMR spectra of a single crystal of $[Fe_3O(O_2CCH_3)_6(3\text{-Cl-py})_3]\cdot 3\text{-Cl-py}$ recorded by using the selective irradiation pulse sequence $90°_x-\tau-180°_y-\tau-90°_y-\tau-180°_y-\tau-$acquire. Turning off the selective pulse on alternate scans and subtracting from memory result in cancellation of all doublets except the selectively irradiated satellite. The echo delay τ was set at 20 μs. There were no selective irradiation and no echo phase cycling for (a). Selective irradiation was performed at the frequencies indicated by the arrows in (b)−(e).

Finally, when the crystal is warmed to the higher temperatures (∼230−300 K), there is now sufficient room for all solvate molecules to become dynamic and as well there can be motion with larger amplitudes. The net result is that the environment about each Fe_3O complex has become averaged out and symmetric in appearance. The potential-energy surface for each Fe_3O complex now has three (or four) minima at the same energy, and each complex can rapidly tunnel between these states. As can be seen in Figures 8 and 10, there is only one type of Fe^{II} signal at 260 K and one average doublet (valence-detrapped) at 293 K (shown as 50% for Fe^{II}_a), whereas the relative occupancies for disordered elements of solvate molecules in positions A and B are not yet equivalent (60/40) at 300 K. It is clear that the solvate molecules play an important role in the overall phase transition and valence-detrapping process in complex **1**.

Magnetic Susceptibility. In Figure 12 are shown plots of the effective magnetic moment versus temperature for both a powder (●) and a single crystal oriented with the *b* axis parallel to the magnetic field (○). There are no detectable changes in magnetic susceptibility correlated with the structural phase transition at ∼200 K. This suggests that the magnetic exchange interactions in complex **1** are relatively insensitive to environment changes. The data for the powdered sample were fitted to the Heisenberg−Dirac−Van Vleck (HDVV) model for a $Fe^{III}_2Fe^{II}$ triangle with $S_1 = S_3 = {}^5/_2$ and $S_2 = 2$. The solid line in Figure 12 represents this least-squares fit. The resulting fitting parameters were found to be $J = -11.5$ cm^{-1}, $J' = -83.5$ cm^{-1}, and $g = 2.00$, where J is the $Fe^{III}-Fe^{III}$ exchange parameter and J' is the $Fe^{II}-Fe^{III}$ exchange parameter. The antiferromagnetic exchange interactions found in this complex are comparable to those found in other mixed-valence Fe_3O complexes. The HDVV model assumes isotropic magnetic exchange interactions. However, the data for the single-crystal sample at low temperatures suggest that there is large magnetic anisotropy.

^{2}H NMR Spectroscopy. ^{2}H NMR spectra were recorded for $[Fe_3O(O_2CCD_3)_6(3\text{-Cl-py})_3]\cdot 3\text{-Cl-py}$ both as a single crystal and as a microcrystalline powder. The goal was to determine whether ^{2}H NMR spectra could detect different Fe_3O complexes in the region where the structural phase transition and valence detrapping occur. Discussion of the factors affecting the ^{2}H NMR spectrum of a paramagnetic compound in the solid state are available.[4a,b,d,15]

Variable-temperature ^{2}H NMR experiments were performed on a 2.0 × 3.5 × 5.0 mm single crystal of complex **1** with CD_3 groups. The CD_3 deuterons serve as a good probe of the complex's electronic structure at temperatures above and below the crystallographic phase transition temperature. The crystal was mounted with the crystallographic *b* axis parallel with the magnetic field direction. When the crystal is oriented in this fashion, four doublets should be seen at 295 K for the different orientations of CD_3 groups. The identification of these four doublets was carried out by selective inversion as described by Wittebort.[16] The dipolar shifts are in the range 5−100 kHz, which is comparable to the quadrupole coupling. In complicated spectra, a straightforward assignment of the doublets is not possible without using two-dimensional techniques or selective excitation. The sequence for refocusing the quadrupole evolution and the dipolar offset is the selective pulse sequence of $90°_x-\tau-180°_y-\tau-90°_y-\tau-180°_y-\tau-$acquire. On alternate repetitions, the selective pulse is turned off and subtracted from memory, leaving only the selectively irradiated doublet. The 90° pulse widths used for the selective and nonselective pulses were 346 μs ($\omega_1/2\pi = 1$ kHz) and 1.8 μs ($\omega_1/2\pi = 277$ kHz), respectively. In Figure 13, trace a is the complete spectrum as obtained using a shift-corrected, nonselective pulse sequence; four well-resolved lines are seen. Traces b−e are the spectra obtained with selective irradiation at the indicated frequencies. This procedure reveals four doublets with quadrupolar splittings of 71.2, 50.3, 0, and 16.6 kHz. The calculated angles and splittings for the high-temperature monoclinic crystal structure are given in a table in the Supporting Information. The experimentally observed splittings and angles are in good agreement.

Spectra for the single crystal were also run in the temperature range of the phase transition. The various peaks broaden and move together as the temperature of the crystal is decreased (figure in the Supporting Information). There does not seem to be any abrupt change in the spectrum at temperatures near the ∼200 K phase transition. The resolution of the spectrum

(15) Mehring, M. *High Resolution NMR in Solids*; Springer-Verlag: New York, 1983.
(16) Wittebort, R. J. *J. Magn. Reson.* **1989**, *83*, 626.

is not good enough to detect crystallographically different Fe_3O complexes. ^2H NMR spectra collected for the powdered sample in the range 295−150 K confirm that the CD_3 groups of the Fe_3O complexes are rotating about their local C_3 axes at rates greater than 10^7 s^{-1}.

Conclusions and Comments

The first case of a crystallographic phase transition associated with the order−disorder conversion of the solvate molecule in a mixed-valence Fe_3O complex has been observed for $[Fe_3O(O_2CCH_3)_6(3\text{-Cl-py})_3]\cdot 3\text{-Cl-py}$ (**1**). At temperatures below ∼200 K a crystal of **1** is triclinic with two different Fe_3O complexes, whereas above ∼200 K it is monoclinic with only one Fe_3O complex. In the layered structure of complex **1** there are only weak van der Waals intermolecular interactions. ^{57}Fe Mössbauer spectroscopy shows that in the range ∼140−260 K the mixed-valence Fe_3O complexes convert from valence-trapped to valence-detrapped. Throughout this range there are two different Fe^{II} Mössbauer signals seen. It was shown that this is a reflection of the order−disorder transformation of the 3-Cl-py solvate molecules.

The crystallographic structural phase at ∼200 K also largely occurs as a result of the onset of disordering in the solvate molecules. Even though this structural change seems to occur abruptly at ∼200 K, the valence detrapping gauged by Mössbauer spectroscopy does not exhibit any discontinuous changes near ∼200 K. The detrapping occurs over a large temperature range (∼200 deg). This is probably not too surprising in view of the apparently weak intermolecular interactions present in the crystal of complex **1**. It would be interesting to determine the heat capacity of complex **1** to see whether heat capacity effects are seen at the ∼200 K structural change and at the ∼260 K culmination of the valence-detrapping process. In other words, it is not totally clear just how many phase transitions occur for the crystal of complex **1**.

Acknowledgment. This work was supported by NSF Grant CHE-9420322 (D.N.H.). D.N.H. thanks the Humboldt Foundation for a Humboldt Forschungspreis in 1993.

Supporting Information Available: Tables of bond lengths, bond angles, anisotropic displacement coefficients, and hydrogen coordinates for the X-ray structures of complex **1** at 300, 228, 200, 169, and 122 K and a figure showing the temperature dependence of the ^2H NMR spectrum for a single crystal of complex **1** (68 pages). Ordering information is given on any current masthead page.

IC9700314